Magnetic correlations, geometrical frustration, and tunable disorder in arrays of superconducting rings

Dragomir Davidović,* Suman Kumar,† and Daniel H. Reich
Department of Physics and Astronomy, The Johns Hopkins University, Baltimore, Maryland 21218

Jeffrey Siegel
Department of Physics, The University of Michigan, Ann Arbor, Michigan 48109

S. B. Field
Department of Physics, Colorado State University, Fort Collins, Colorado 80523

R. C. Tiberio
Cornell Nanofabrication Facility, Cornell University, Ithaca, New York 14853

R. Hey and K. Ploog
Paul-Drude-Institut für Festkörperelektronik, D-10117 Berlin, Germany
(Received 9 July 1996)

A superconducting ring, biased in an external flux $\Phi_0/2$, can be in either of two energetically degenerate fluxoid states. In one state, the supercurrent flows in a clockwise direction with a resulting downward magnetic moment; the current in the other state flows in a counterclockwise direction and its moment points up. There is thus a strong analogy between such a ring and an Ising spin. Two nearby but electrically isolated rings can interact magnetically; this interaction favors an antiparallel alignment of moments and is thus analogous to an antiferromagnetic spin-spin interaction. Regular arrays of such rings may thus be expected to exhibit effects of lattice geometry and geometrical frustration. To study these issues, we have fabricated arrays containing up to 2.4×10^5 aluminum rings, each approximately 1.6 μm across. We have used a sensitive superconducting quantum interference device-based magnetometer to probe the global magnetic properties of the arrays; local information about particular spin configurations was obtained using a high-resolution scanning Hall probe microscope. The magnetic measurements show that individual rings do indeed behave as Ising spins, showing a paramagnetic susceptibility which freezes out only a few milliKelvin below the critical temperature T_c. This illustrates that the ring dynamics is dominated by an energy barrier between the two states which rises rapidly as the temperature is lowered below T_c. The magnetic measurements also show a hysteretic field dependence of the susceptibility which can be quantitatively interpreted in terms of an antiferromagnetic interaction between the rings. To explore possible ordering of the spins, we have used the Hall microscope to directly image specific configurations of spins. We find significant antiferromagnetic nearest-neighbor correlations, but no evidence for any long-range ordering. We attribute this to a significant degree of disorder in the system related to small fluctuations in the areas of the aluminum rings. The effective disorder may be increased by working at higher fractions of Φ_0. The observed short-range correlations drop rapidly at these higher fractions. [S0163-1829(97)01710-4]

I. INTRODUCTION

An array of closely spaced but electrically isolated superconducting rings forms a novel type of extended superconducting microstructure.[1] Unlike Josephson-junction arrays or wire networks where the individual elements of the array are coupled directly through the superconducting order parameter, isolated rings can only couple magnetically. In an applied flux near $\Phi_0/2$ the rings behave like Ising spins and a ring array becomes a model two-dimensional (2D) Ising antiferromagnet. In this paper we describe experiments on arrays of micron-size aluminum rings that demonstrate this Ising spin analogy, and show that the distribution of flux quanta in the array is influenced by the interactions between the rings.

The Ising spin analogy arises because in an applied magnetic flux Φ near $\Phi_0/2$, a superconducting ring has two states that are close in energy. One of these states contains zero fluxoid quanta $(n=0)$, and the other contains one fluxoid quantum $(n=1)$. The induced supercurrents in these two states flow in opposite directions, and the ring's magnetic moment points either along the applied field or against it. For $\Phi<\Phi_0/2$ the $n=0$ state is energetically favored, and for $\Phi>\Phi_0/2$ the $n=1$ state is favored. Exactly at $\Phi_0/2$, they are energetically degenerate. Because the $n=0$ state has its magnetic moment antiparallel to the field we label it ''spin down;'' likewise, because the moment of the $n=1$ state is parallel to the field, we call this state ''spin up.'' At low temperatures, the fluxoid state of the ring cannot change—the familiar case of flux trapping—and the spin is ''frozen,'' but as we shall see, very close to T_c flux quanta move in and out of the ring in a thermally activated fashion, and the ring

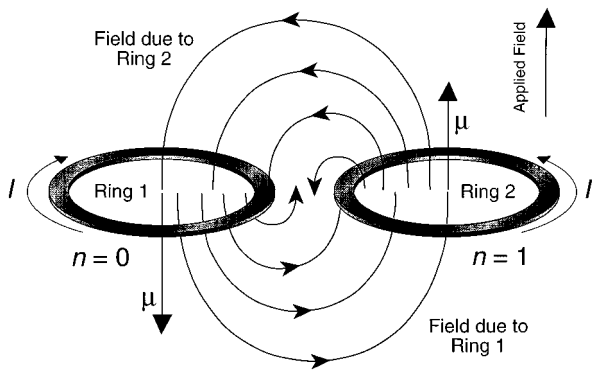

FIG. 1. Shown are two nearby rings in an applied flux of $\Phi_0/2$. Ring 1, with its current I and moment μ as shown, generates a dipole magnetic field pointing *up* at ring 2. Thus the flux through ring 2 is greater than $\Phi_0/2$, stabilizing it in the ''spin up'' configuration. The dipole field from ring 2 then points down at ring 1; this stabilizes ring 1 in its downward orientation. Thus it is energetically favorable for the two rings to have opposite spin orientations, i.e., the rings have an *antiferromagnetic* coupling.

can flip between spin up and spin down. It is in this region where the inter-ring interactions can have an influence, and possible cooperative effects can occur.

To see how the rings can interact, consider two superconducting rings in close proximity in an applied flux of $\Phi_0/2$, as illustrated in Fig. 1. The induced supercurrent in each ring generates an additional magnetic flux through the other ring; this is the source of the magnetic interaction. Suppose the first ring is spin down, with its moment antiparallel to the applied field H. Because of the dipolar nature of the field a ring generates, the additional field from the first ring makes the net flux through the second ring larger than $\Phi_0/2$, and biases it into the spin up state. The field from the second ring then reduces the flux through the first ring to less than $\Phi_0/2$, favoring its spin down state. There is thus a net antiferromagnetic (AFM) interaction between any pair of rings, and an array of rings may be thought of as a two-dimensional Ising antiferromagnet.

Because such a ''spin system'' is made lithographically, one has considerable freedom in its design, and this opens up the possibility of doing detailed experimental tests of important questions in magnetism involving the effects of lattice geometry and geometrical frustration on antiferromagnetic ordering. This paper describes experiments on arrays of micron-sized aluminum rings using superconducting quantum interference device (SQUID) susceptometry and scanning Hall probe microscopy to probe the rings' dynamics and correlations. We find that there are significant short-range antiferromagnetic correlations in all the arrays studied. There is no long-range order, however, even on bipartite lattices. This is due to quenched disorder, which arises from slight variations in the rings' areas. These variations lead to slightly different fields for a half a flux quantum for different rings. This amounts to an effective random field, and the arrays are therefore random field Ising antiferromagnets. At the temperature where the spins freeze and can no longer flip, the magnetic interactions are not strong enough to overcome the random field, and only short-range correlations can be established. Nevertheless, we were able to observe a reduction in the antiferromagnetic correlations on the geometrically frustrated triangular and kagomé lattices as compared to the unfrustrated honeycomb and square lattices.

This paper is organized as follows. Section II explains the analogy between Ising spin systems and the superconducting ring arrays in more detail, and describes the appropriate model for the arrays: interacting classical two-level systems in a random field plus an external field. Section III describes the fabrication of the arrays and the measurement techniques used. Section IV presents magnetization and susceptibility measurements, and Sec. V presents magnetic images of the ring arrays.

II. THEORY

A. Superconducting rings as Ising spins

We are interested in the properties of arrays of superconducting rings near T_c, where the rings' moments can flip freely. Near T_c, the properties of a superconducting ring may be calculated from Ginzburg-Landau (GL) theory. A detailed calculation for the rings in this experiment is given in Appendix A; here we discuss some of the main results. In thermal equilibrium, rings will tend to populate states with the lowest free energy F. Figure 2(a) shows $F(\Phi)$ at four temperatures near $T_c(\Phi_0/2)$, for a ring in either the $n=0$ or $n=1$ state. In this calculation we have used parameters appropriate for the aluminum rings used in our experiments. There is a local minimum in $T_c(\Phi)$ at $\Phi_0/2$ (the Little-Parks effect[2]), and thus as the curves for $T_c(\Phi_0/2)+3$ mK show, above $T_c(\Phi_0/2)$ there is a region near $\Phi_0/2$ where there is no superconducting state. At $T_c(\Phi_0/2)$ the $n=0$ and $n=1$ curves first meet, and at that temperature and below, the two states are degenerate at $\Phi_0/2$. If we move slightly away from $\Phi_0/2$, then the free energy may be written $F_\pm = F(\Phi_0/2) - (H - H_{1/2})\mu_\pm$, where $\mu_\pm = -\partial F_\pm / \partial H$ is the magnetic moment of the ring in the up $(+)$ or down $(-)$ state, and $H_{1/2}$ is the magnetic field required to apply a flux $\Phi_0/2$ to the ring. $F_\pm$ thus has the form of a Zeeman energy. μ is plotted in Fig. 2(b). Note that the moments in the up and down states at $\Phi_0/2$ are not the same. This arises from a nonuniform current density in the ring, and will be seen directly in measurements to be discussed in Sec. IV. At $\Phi_0/2$, although $\mu_+ \neq \mu_-$, in our calculation the *total* current I flowing in the two states is equal, as may be seen in Fig. 2(c). We also note that near $T_c(H)$, $F \sim [1 - T/T_c(H)]^2$, $I \sim 1 - T/T_c(H)$, and $\mu \sim 1 - T/T_c(H)$, which means that the magnetic moment of the Ising spins is temperature dependent.

The essential physics of the ring arrays near $\Phi_0/2$ (or any odd half-integer multiple of Φ_0) is contained in the antiferromagnetic Ising Hamiltonian

$$\mathcal{H} = \sum_{i \neq j} V_{ij} s_i s_j - \sum_i (H - H^i_{1/2}) \mu(s_i) s_i , \qquad (2.1)$$

where V_{ij} is the magnetic coupling energy between rings at sites i and j, $s_i (= \pm 1)$ is the Ising variable assigned to ring i, and $H^i_{1/2}$ is the magnetic field needed to produce $\Phi_0/2$ in ring i. The coupling energy is $V_{ij} = M_{ij} I_i I_j$, where M_{ij} is the mutual inductance. Since the currents in the two spin states

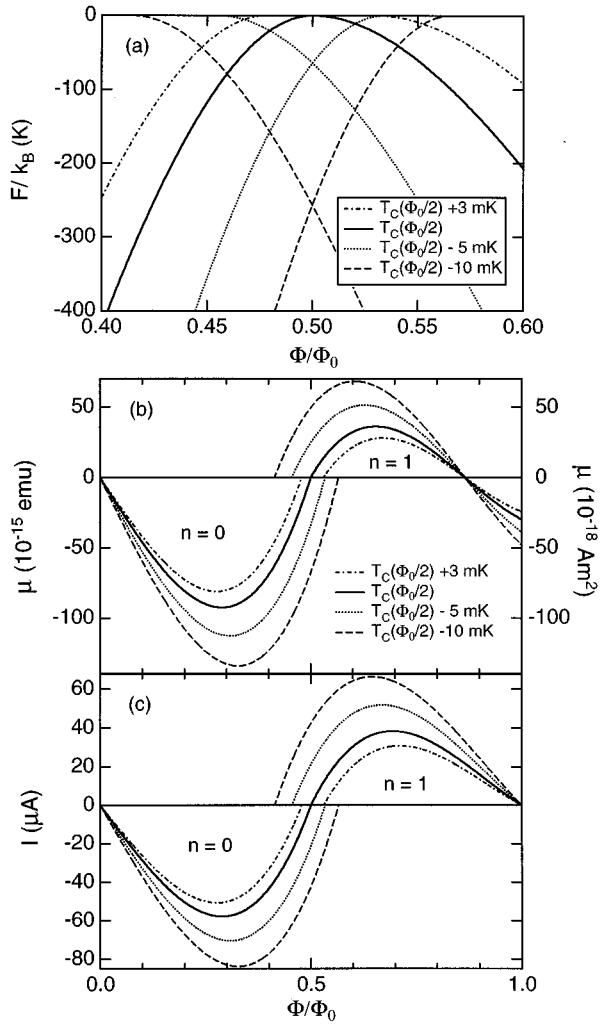

FIG. 2. Calculated properties of a square superconducting ring near $T_c(\Phi_0/2)$ with dimensions the same as those measured. (a) Superconducting free energy relative to normal state. Curves with positive slope are for $n=0$ state, and curves with negative slope are for $n=1$ state. (b) Magnetic moment of ring. (c) Total current flowing in ring.

are the same, we can write $I_i = Is_i$, and $V_{ij} = M_{ij}I^2$. Note that this coupling is *temperature dependent*.

B. Random field

In a real ring array, there will be small random variations in the effective areas A_i of the rings, due to imperfections in the fabrication process. Since $H^i_{1/2} = \Phi_0/2A_i$, this will lead to small variations in the flipping fields $H^i_{1/2}$ from ring to ring. This randomness turns out be very important in determining the ground state configuration of the arrays. Its effect is illustrated in Fig. 3(a). Here, the ring on the left has a slightly smaller area than the ring on the right. Thus, $H_{1/2}$ for the first ring is larger than $H_{1/2}$ for the second ring. It is then possible to apply a magnetic field that generates a flux smaller than $\Phi_0/2$ in the first ring, but larger than $\Phi_0/2$ in the second ring. In such a field, the first ring will tend to cool down in the spin-down state, and the second ring will tend to cool down in the spin-up state.

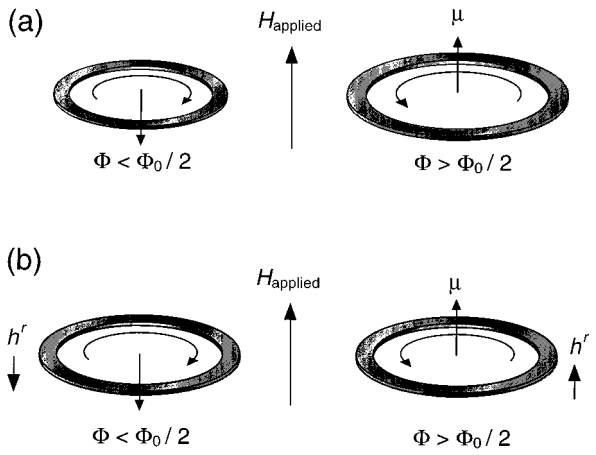

FIG. 3. Due to imperfections in their fabrication, different rings in the array will have slightly different areas (here greatly exaggerated). (a) The applied field is such that the flux through the left ring is less than $\Phi_0/2$, stabilizing it in a down-spin orientation, while the flux through the right ring is greater than $\Phi_0/2$, stabilizing its spin in an upward direction. (b) The situation in (a) is equivalent to rings of equal areas, but acted upon by a small random field component h^r in addition to the applied field; h^r points downward for smaller-than-average rings, and upwards for larger-than-average ones.

The physics of this situation is identical to one wherein the rings are *identical*, but each has a small extra field h^r applied to it [Fig. 3(b)]. This field points parallel to H for the right-hand ring, yielding a slightly larger flux than average; similarly, it points opposite to H for the left-hand ring, producing a smaller-than-average flux. The effect of this will be a tendency for each ring to polarize in the direction of its local extra field. For an array of rings, weak disorder in the ring areas can thus be modeled by a *random field* term, $-\sum\mu(s_i)h^r_i s_i$, where h^r_i is a fixed random field, which can be described by some statistical distribution function. For the rings studied here, a Gaussian distribution of h^r_i is satisfactory. For a particular ring in the array, h^r_i is the field that corresponds to the difference between the field $H^i_{1/2}$ for that ring and the array-averaged value of $H_{1/2}$, which we will denote by $\overline{H_{1/2}}$. The Hamiltonian for the ring arrays then becomes the random-field Ising model[3]

$$\mathcal{H} = \sum_{i\neq j} V_{ij}s_i s_j - \sum_i \mu(s_i)(h + h^r_i)s_i , \qquad (2.2)$$

where the effective external field is $h = H - \overline{H_{1/2}}$. It has been shown that the lower critical dimension for the random field Ising model is $D=2$,[4] and that the ground state in a weak random field is broken into domains of Néel order. It turns out for our ring arrays that in the temperature range where the rings can flip, the random field term and the interaction term are of the same order of magnitude and only near-neighbor correlations are measurably different from zero.

C. Ring dynamics

The dynamics of the Ising model in Eq. (2.2) is determined by the energy barrier between the rings' spin-up and spin-down states. Unlike spins in conventional magnetic ma-

TABLE I. Parameters of square and hexagonal rings. $H_{1/2}$ is field for $\Phi_0/2$. $\tilde{I}$, $\tilde{J}$, and $\tilde{K}$ are defined in Appendix A. For our square rings $a=0.8$ μm, and $b=1.6$ μm. For our hexagonal rings $a=0.538$ μm, and $b=1.0$ μm.

	Square	Hexagon
$H_{1/2}$	$[\Phi_0\ln(b/a)]/(b^2-a^2)$	$[2\Phi_0\ln(b/a)]/[3\sqrt{3}(b^2-a^2)]$
$\tilde{I}(n,H)$	$(n^2/8)\ln(b/a)-n[H(b^2-a^2)]/(8\Phi_0)$ $+[H^2(b^4-a^4)]/(32\Phi_0^2)$	$[n^2/(4\sqrt{3})]\ln(b/a)-n[3H(b^2-a^2)]/(8\Phi_0)$ $+[27H^2(b^4-a^4)]/(64\sqrt{3}\Phi_0^2)$
$\tilde{J}(n,H)$	$(n/8)\ln(b/a)-[H(b^2-a^2)]/(16\Phi_0)$	$[n/(4\sqrt{3})]\ln(b/a)-[3H(b^2-a^2)]/(16\Phi_0)$
$\tilde{K}(n,H)$	$[(b^2-a^2)/16]\{n-[H(b^2+a^2)]/(2\Phi_0)\}$	$[3(b^2-a^2)/16]\{n-[3\sqrt{3}H(b^2+a^2)]/(4\Phi_0)\}$
calculated $H_{1/2}$	7.48 G	6.95 G
measured $H_{1/2}$	7.53 G	6.98 G
measured $\xi(0)$	0.24 μm	0.235 μm

terials, the spin state of a superconducting ring involves a macroscopic number of particles. To change the spin state of a ring, a flux quantum must move in or out of it, which means that it is necessary to break all the Cooper pairs that are contained in a volume of order $dw\xi$, where d and w are the wire thickness and width, respectively, and ξ is the GL coherence length. This leads to a *temperature-dependent* energy barrier $E_B\sim|\epsilon_c|dw\xi\sim[1-T/T_c(\Phi_0/2)]^2$ between the two spin states,[5] where ϵ_c is the condensation energy. The frequency of thermally induced spin transitions is then

$$\Gamma=\Omega e^{-E_B/k_BT}, \tag{2.3}$$

where Ω is an attempt frequency. In most of the superconducting phase diagram this barrier is so large that a ring never spontaneously flips its spin. The only exception is very near T_c, and very near $\Phi_0/2$ (or any other half-integer fraction), when the energy barrier becomes small enough so that spontaneous spin transitions can take place. However, since E_B rises rapidly as T is lowered below T_c, and Γ depends exponentially on E_B, there is a rather well-defined temperature T_f where the rings' moments will freeze out.

The energy barrier between different fluxoid states that is appropriate for a ring with circumference L much longer than the coherence length was originally calculated by Langer and Ambegaokar.[5] They assumed that during the transition the order parameter passes through a saddle point of the free-energy functional. The saddle point functions also satisfy the GL equations, and the energy barrier is the difference between the energies of the fluxoid states and the energy of the saddle point solutions. For an infinitely long wire, this energy barrier is $E_B=3.77|\epsilon_c|wd\xi$. Using time-dependent GL theory, McCumber and Halperin[6] determined the attempt frequency to be

$$\Omega=\frac{L}{\xi}\sqrt{\frac{E_B}{k_BT}}\frac{1}{\tau_s}, \tag{2.4}$$

where $\tau_s=\pi\hbar/8k_B(T_c-T)$ is the relaxation time of the superconductor. Tarlie *et al.*[7] have extended the calculation of the energy barrier to rings with smaller values of L/ξ. Our measurements of the frequency dependence of the ac susceptibility (Sec. IV B) show that the barrier is $E_B\approx|F|/3$, where F is the total superconducting free energy of the $n=0$ or $n=1$ state. Although the saddle point solutions have not been examined exhaustively to find the minimum barrier height, there is one such state that gives good quantitative agreement with our data.[8] This will be described in more detail in Sec. IV B. In the discussions that immediately follow, we will estimate the flipping rates taking $E_B\approx|F|/3$ with Ω given by Eq. (2.4), and assuming that $\tau_s=\pi\hbar/8k_B[T_c(H)-T]$.

D. Estimate of the Néel ordering temperature

We now estimate the ordering temperature T_N for the Ising transition in a bipartite superconducting ring array, neglecting the random field. We show that this temperature is well above the freezing temperature T_f; this gives us confidence that, absent any randomness, the Néel state is experimentally accessible. As is well known,[9] for the near-neighbor Ising model, T_N occurs at $k_BT_N=2.27V_{ij}$ for the square lattice, and at $k_BT_N=1.52V_{ij}$ for the honeycomb lattice. Unlike the usual Ising model, however, for the rings the interaction strength V_{ij} is temperature dependent. From Eq. (A10), the temperature dependence of the rings' supercurrents near $T_c(\Phi_0/2)$ is

$$I_i=I(0)\left(1-\frac{T}{T_c(\Phi_0/2)}\right), \tag{2.5}$$

where $I(0)$ can be obtained from Eq. (A10) and Table I. The ring-ring interaction is then

$$V_{ij}(T)=V_{ij}^0\left(1-\frac{T}{T_c(\Phi_0/2)}\right)^2, \tag{2.6}$$

with $V_{ij}^0=M_{ij}I^2(0)$. Therefore, as T decreases, the coupling energies increase very rapidly. The near-neighbor mutual inductance for both our square and honeycomb arrays is about

68 fH. The current prefactor is $I(0)\approx 5$ mA. The near-neighbor interaction is then $V_{\rm NN}^0 = 1.7\times 10^{-18}$ J. Hence, $1-T_N/T_c(\Phi_0/2)\approx 2\times 10^{-3}$ for the square lattice, and $1-T_N/T_c(\Phi_0/2)\approx 2.5\times 10^{-3}$ for the honeycomb lattice. The magnetic ordering temperatures are thus very close to $T_c(\Phi_0/2)$.

To observe the ordered spin state experimentally, the temperature T_f when the individual rings freeze must be below T_N. Because the flipping is thermally activated, as shown by Eq. (2.3), the freezing of the individual rings occurs much more rapidly than the increase of the ring interactions. We can estimate the flipping rate at T_N, taking $E_B\approx|F|/3$ as outlined in the previous section. From Appendix A, for the square lattice the free energy per ring is $F\approx 5.06\times 10^{-17}[1-T/T_c(\Phi_0/2)]^2$ J. Note that this is much larger than the coupling energy V. Then, $E_B(T_N)/k_BT_N\approx 4.2$, and $\Gamma\approx 1.6\times 10^8$ Hz. Thus, the correlated state could easily be realized in experimental time scales if the random field were not present. Similarly, for the honeycomb lattice, we find that at the Ising transition $\Gamma\approx 3\times 10^7$ Hz.

For Ising spins on nonbipartite lattices, such as the kagomé and triangular lattices, the ground state is not unique[10] and there is no long-range antiferromagnetic order. The absence of long-range order originates from geometrical frustration. The magnetic behavior of the ring arrays on these lattices should be different from the magnetic behavior of bipartite ring lattices. Direct observations of spin correlations, using the scanning Hall microscope technique, will be described in Sec. V.

III. FABRICATION AND MEASUREMENT TECHNIQUES

A. Ring array fabrication

Our main goal in designing the ring lattices was to maximize the magnetic coupling between the rings at the freezing temperature. Thus the parameter to be maximized is the ratio of the ring-ring coupling energy V to the energy barrier E_B. Both E_B and V are temperature dependent, but their ratio is not. Using Table I, Eqs. (A7) and (A10), and taking $E_B\approx|F|/3$, we find that this ratio is approximately

$$\frac{V}{E_B}\approx 3\pi\left(\frac{\xi}{\lambda}\right)^2\frac{wdMc^2}{L^3}, \tag{3.1}$$

where λ/ξ is the Ginzburg Landau parameter. To maximize ξ/λ, we chose aluminum, because it is a strongly type-I superconductor. The ratio $wdMc^2/L^3$ depends only on the rings' geometry. We calculated M numerically, assuming that the current density distribution is given by Eq. (A2), although the result obtained assuming a uniform current density is not appreciably different. M is a decreasing function of w and d, and an increasing function of L, but these dependences are weaker than the prefactor wd/L^3. To maximize V/E_B the rings should therefore have small circumference and large thickness and width. Of course, to maximize M the rings should be as close together as possible.

Figure 4 shows scanning electron microscope (SEM) images of the four basic lattices that we constructed: honeycomb, kagomé, square, and triangular. Note that in the honeycomb, kagomé, and triangular lattices the rings' dimensions and near-neighbor spacings are identical, and so, presumably, are the near-neighbor couplings. Only the lattice connectivity is changed. We can also hold the ring size and lattice connectivity constant, and vary the inter-ring spacing. The inset to Fig. 4 shows a portion of a ''sparse'' array of square rings identical to those in the square lattice in Fig. 4.

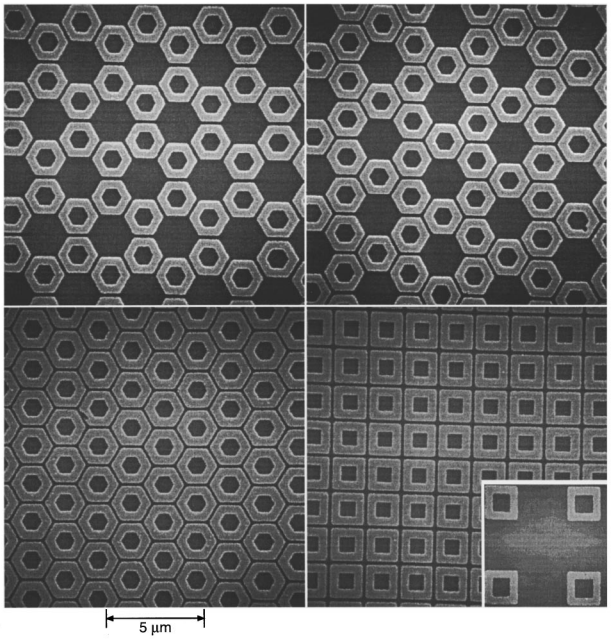

FIG. 4. SEM micrographs of arrays of aluminum rings. All rings have 0.4 μm linewidth and are 0.24-μm thick. Top left: honeycomb lattice; top right: kagomé lattice; bottom left: triangular lattice; bottom right: square lattice. Inset: unit cell of a ''sparse'' array of square rings used to study effect of interring separation on interactions.

To maximize the mutual inductance on the densely-packed lattices, the rings were made in square or hexagonal shapes. The outer sides of the square rings are 1.6 μm and the outer sides of the hexagonal rings are 1 μm. For both shapes, the wire widths are 0.4 μm, the film thicknesses are 0.23 μm and the gap between rings is 0.2 μm. For the sparse square array shown in the inset to Fig. 4, the gap between the rings is 2.4 μm. Assuming that the current distribution in the rings is given by Eq. (A2), the self inductance of both the square and the hexagonal rings is $L_s\approx 1.6$ pH. For the square lattice in Fig. 4, the first, second, and third nearest-neighbor mutual inductances are 68, 18, and 4 fH, respectively. Very similar numbers were obtained in a calculation with uniform current densities. The near-neighbor coupling between the rings in the sparse array is 18 times smaller than the coupling between the closely spaced rings. For the three hexagon ring lattices, the first and second nearest-neighbor mutual inductances are 68 and 4 fH, respectively.

The ring arrays were produced at the Cornell Nanofabrication Facility. They were made on sapphire substrates by electron beam lithography using a single layer resist, followed by e-beam evaporation of the aluminum and lift off. The dense square arrays had 160 000 rings, and the honeycomb, kagomé, and triangular lattices had 170 000, 182 000, and 243 000 rings, respectively. The sparse square arrays had 40 000 rings.

B. SQUID Magnetometer

The magnetic moment and ac susceptibility $\chi(H,T)$ of the arrays was measured as a function of dc field H and temperature T with a SQUID magnetometer mounted on a dilution refrigerator. H and the ac measuring field H_{ac} were produced by separate superconducting solenoids. The dc magnet was operated in persistent mode to produce a stable field, and to provide magnetic shielding. Induced currents in a gradiometer consisting of a pair of five-turn pickup coils (radius 0.5 cm) were measured with a commercial (BTI) dc SQUID. Additional magnetic screening was provided by Pb and μ-metal shields.

The sample was mounted on a sapphire rod and placed in the center of one of the pickup coils. The rod was heat sunk to the mixing chamber of the dilution refrigerator. Temperature stability of ± 20 μK was achieved with a Lakeshore Cernox thermometer mounted on the mixing chamber, using a commercial resistance bridge and temperature controller. With $H_{ac}=6$ mG rms at frequency $f=3$ Hz, the ac response was linear for all H and T, and the total ac moment produced by the arrays was $\approx 1\times 10^{-9}$ emu for $T \ll T_c$. The low frequency sensitivity of the gradiometer was 10^{-11} emu/$\sqrt{\text{Hz}}$.

C. Scanning Hall probe microscope

The low-temperature spin configurations of the arrays were imaged using a scanning Hall probe microscope.[11] Scanning Hall probe microscopy (SHM) is a technique suitable for spatial imaging of magnetic fields with micron spatial resolution.[12] A similar microscope has been used to image vortices in superconducting wire networks.[13] The Hall probe is made of a GaAlAs/GaAs heterostructure patterned into a Hall geometry by photolithography. The size of the Hall probe is 1×1 μm. The active area of the probe is within ≈ 7 μm of the corner of the GaAs chip; this allows the probe to be brought very close (≈ 0.5 μm) to the upper surface of the rings. This close approach is necessary to obtain high spatial resolution and large field modulations.

The microscope's scan range at 4.2 K is approximately 150×150 μm. The sensitivity of the Hall probe is about 5 mG/$\sqrt{\text{Hz}}$. The Hall voltage was measured using a digital lockin amplifier at $f=1$ kHz, with a 3-ms time constant. The entire microscope was attached to a ^{3}He cryostat, and could be easily cooled from above T_c to about 650 mK where the images were taken.

IV. MAGNETIC MEASUREMENTS

In this section we describe magnetic measurements made on the arrays with the SQUID magnetometer. Several types of measurements were performed. From measurements of the dc magnetic moments of the arrays as a function of temperature and field, we show that individual rings do indeed behave like Ising spins. We then probe the *dynamics* of the rings using the temperature dependence of the ac susceptibility. Such measurements clearly show the freezeout of the spins as the temperature is lowered only slightly below T_c. Finally, from the field dependence of the ac susceptibility we can obtain information about the magnitude and sign of the inter-ring magnetic interactions.

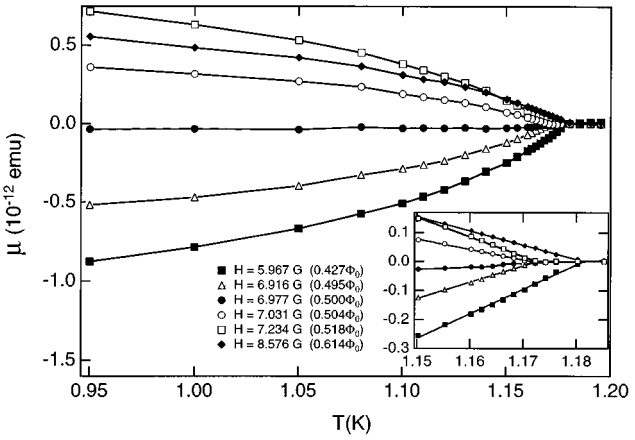

FIG. 5. Field-cooled dc magnetic moment per ring μ vs temperature for a kagomé lattice in the region around $\Phi_0/2$ applied flux per ring. Inset shows linear dependence of μ on T very near T_c.

A. Magnetic moment measurements

Figure 5 shows the magnetic moment per ring μ as a function of temperature near T_c for a kagomé lattice of hexagonal rings. The rings were cooled in a fixed applied magnetic field H. The average field for half a flux quantum for this array is $H_{1/2}=6.977$ G, as determined from SHM measurements (Sec. V B). If H is less than $H_{1/2}$, μ is negative indicating that a majority of the rings are in the $n=0$ state with their spins pointing in the direction opposite to the applied field. If H is greater than $H_{1/2}$, μ is positive and a majority of the rings are in the $n=1$ state with their spins pointing parallel to the field. If $H=H_{1/2}$, practically no net magnetic moment appears below T_c. This occurs because half of the rings in the array cool into the spin up state and half cool into the spin down state. Note that the value of $H_{1/2}$ value agrees very well with the calculated value $H_{1/2}=6.95$ G (see Table I).

The inset to Fig. 5 shows that very near $T_c(\Phi_0/2)$ the average magnetic moment per ring, and thus the average current per ring, is a linear function of T. One can also see the minimum in T_c at $\Phi_0/2$, characteristic of the Little-Parks effect.[2] We can calculate the coherence length by comparing the measured $T_c(H)$ to the predictions of GL theory. We obtain $\xi(0)=0.235$ μm, which is a typical value for thin Al films. All of the arrays that we measured showed similar effects. Table I summarizes these results for both the square and hexagonal rings.

We also find that the magnetic moment in the spin down state μ_- is noticeably larger than the magnetic moment in the spin up state μ_+, consistent with the GL analysis summarized in Fig. 2. This can be seen most clearly by comparing the data at 0.495 Φ_0 and 0.504 Φ_0 in Fig. 5. This asymmetry arises because in a ring with finite wire width, the current distributions are different in the up and down states. The measured ratio of the magnetic moments in the spin up and the spin down states is $|\mu_+/\mu_-|=0.69$ just below T_c. In our approximate calculation within GL theory (see Table I and Fig. 2), the total currents flowing in the two states of a ring are identical in magnitude, but the magnetic moments are not. For the hexagonal rings our calculation gives $|\mu_+/\mu_-|=0.78$.

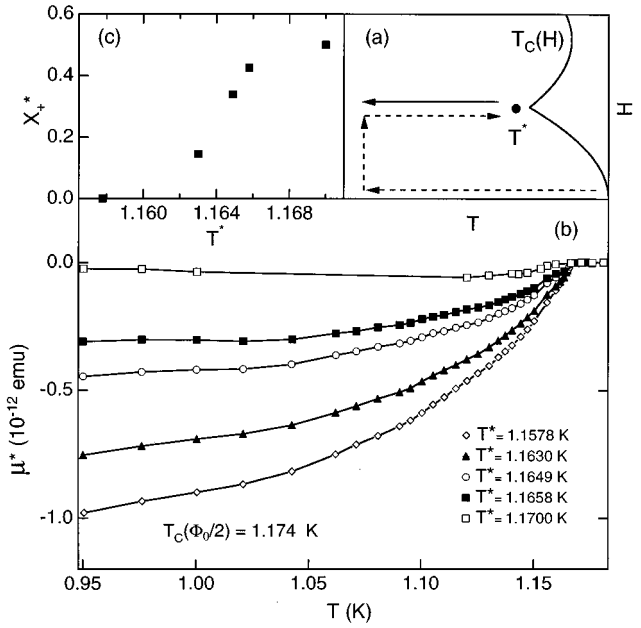

FIG. 6. Determination of temperature range where rings can flip. (a) Dashed arrows: path in H-T plane traversed by array to first prepare it in a state with all rings spin down, and then to warm to $T^\star$ to allow rings to flip. Solid arrow: line along which $\mu(T)$ shown in (b) was measured. (c) Fraction of rings that flipped from spin down to spin up for different $T^\star$.

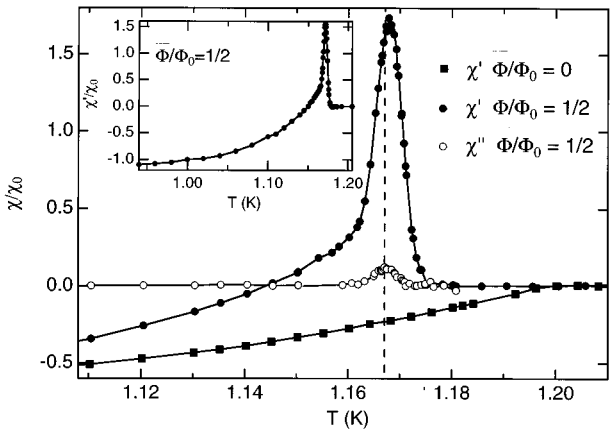

FIG. 7. ac susceptibility χ of kagomé and triangular (inset) ring arrays near T_c. In zero applied dc flux, only a diamagnetic response is observed. At $\Phi_0/2$, a large paramagnetic spike in χ' appears as the rings flip in response to the ac field. The freezing temperature T_f (dashed line) is defined by the peak in χ'' (open circles). The data are normalized to χ_0, the value of χ at $T=1$ K.

At low temperatures, the magnetic moment per ring is nearly temperature independent. Using Table I we can calculate the current corresponding to the measured magnetic moment, and hence estimate the self-induced flux in a ring. At $T=0.95$ K, we find that $\Phi=L_sI=0.45\Phi_0$, which is approaching the perfectly screened limit of 0.5 Φ_0.

Magnetization measurements can also give us the range of temperatures near $T_c(\Phi_0/2)$ where the rings can flip. To do this, the rings were first cooled down to 0.95 K in zero field, as sketched in Fig. 6(a). In this way, all the rings were trapped in the $n=0$ state. The applied field was then set to $H_{1/2}$. Since the rings are strongly hysteretic at this low temperature, no rings flipped when the field was increased. Next, the temperature was increased to some value $T^\star<T_c(\Phi_0/2)$. This was done carefully, making sure that the temperature was always less than or equal to $T^\star$. The rings were kept at $T^\star$ for one minute, and then they were cooled back to 0.95 K while the magnetic moment was measured. Figure 6(b) shows the magnetic moment per ring measured in this way for a kagomé array. Initially at $T=0.95$ K and $H=H_{1/2}$, all the rings are in the spin down state with magnetic moment μ_-. After cycling to $T^\star$ and back, some of the rings have flipped, and the average moment per ring is $\mu^\star=x_+^\star\mu_+ +(1-x_+^\star)\mu_-$, where $x_+^\star$ is the fraction of the rings that flipped to the up state at $T^\star$. Solving for $x_+^\star$ gives

$$x_+^\star=\frac{1-\mu^\star/\mu_-}{1-\mu_+/\mu_-}. \tag{4.1}$$

$\mu^\star/\mu_-$ is obtained from the data in Fig. 6, and $\mu_+/\mu_-=-0.73\pm0.01$ at 0.95 K from the data in Fig. 5. The results for $x_+^\star$ vs $T^\star$ are shown in Fig. 6(c). We see that at $T^\star=1.170$ K, $x_+^\star=0.5$ which means that the energy barrier between the up and down states has been reduced sufficiently to allow the rings to reach thermal equilibrium. This temperature is about 4 mK below $T_c(\Phi_0/2)$. As $T^\star$ is reduced, however, $x_+^\star$ drops rapidly to zero; for $T^\star<1.158$ K no rings could flip. Thus there is only a narrow temperature region within about 10 mK of T_c where the energy barrier is small enough to allow the rings to reconfigure thermally. This is a crucial result, and should be born in mind in all subsequent discussion. Notice that the freezing process is gradual as the temperature decreases. This suggests that the spin freezing temperature is not the same for each ring, i.e., that there is a distribution of thermal relaxation times.

B. ac susceptibility: temperature dependence

By measuring the ac susceptibility $\chi(H,T)$, we could probe the rings' dynamics directly. This section describes the temperature dependence of the susceptibility at fixed field, which gives us quantitative information on the average dynamic response of individual rings.

To measure $\chi(H,T)$, a magnetic field $H(t)=H+H_{\rm ac}\cos\omega t$ was applied to the sample, and the resulting ac response from the SQUID was measured with a lockin amplifier. The dc field H was typically near the field corresponding to $\Phi_0/2$ (7.0 or 7.5 G), and $H_{\rm ac}$ was typically 6 mG rms.

Figure 7 shows the temperature dependence of the real part of the susceptibility χ' for the hexagonal rings at $\omega/2\pi=3$ Hz in average applied fluxes $\Phi=0$ and $\Phi=0.5$ Φ_0. Φ is defined such that $\Phi=\Phi_0/2$ when half the spins are up and half down in a field-cooled magnetization (Fig. 5) or SHM (Fig. 19) measurement. The main part of the figure shows data for a kagomé lattice very near T_c, and the inset shows data for a triangular lattice over a broader temperature range. At zero flux per ring the ac susceptibility in the superconducting state is negative. This differential Meissner effect arises as the ac flux is screened from passing through

the rings. At $\Phi_0/2$, however, the χ' vs T curve is very different: there is a dramatic paramagnetic spike in χ' just below T_c. Then, as the temperature is decreased further χ' becomes negative, and the differential Meissner effect is recovered.

The paramagnetic signal in χ' at 0.5 Φ_0 occurs precisely in the temperature range where the $\mu(T)$ measurements show that the rings can reorient. It arises because the rings are switching between the $n=0$ and $n=1$ fluxoid states in response to the ac field. This flipping leads to a paramagnetic response, just as for spins in a magnetic system. Unlike ordinary spins, however, the temperature dependence of the rings' magnetic moment $\mu \propto 1-T/T_c$ leads to a much faster rise in χ than the usual Curie-type response. At first glance, the peak in χ' might appear to signify a cooperative ordering transition. However, we observed this peak in all of the arrays, irrespective of lattice geometry or inter-ring separation.[14] The peak is in fact a single-ring effect that reflects the temperature dependence of the rings' dynamics.

As for any two-level system[15] the dynamics are determined by the transition rate Γ [Eq. (2.3)] between the two states. For the rings, the dominant influence on Γ is the temperature dependence of E_B, $E_B \sim [1-T_c/T_c(\Phi_0/2)]^2$ (see Sec. II C). Just below T_c when E_B is small, Γ is large. When $\Gamma \gg \omega$, the population of up and down spins stays in thermal equilibrium as the ac field changes, and the ac response measures the dc, or isothermal, susceptibility. However, as E_B grows with decreasing temperature, Γ decreases extremely rapidly. When $\Gamma \approx \omega$, the amplitude of χ' drops and a phase shift marked by a peak in χ'' appears, as shown in Fig. 7. The temperature of the peak in χ'' defines the freezing temperature T_f at frequency ω (dotted line). As E_B grows further at lower temperatures, Γ becomes much smaller than ω. Then the rings can no longer flip in response to $H_{\rm ac}$, and that contribution to χ is suppressed. There is a second contribution to the ac susceptibility, however, which is equal to the field derivative of the magnetic moment of the rings trapped in the up and/or down states. We see from Fig. 2(b) that near $\Phi_0/2$, the slope of the μ vs Φ curve is *positive*. This ''adiabatic susceptibility'' thus gives rise to the residual *paramagnetic* tail in $\chi(T)$ below the peak.

Because of the strong T dependence of E_B, the transition from dynamic to frozen spins happens in a region only a few mK wide. Nonetheless, the frequency dependence of T_f characteristic of this type of dynamic freezing can be observed. The frequency dependence of χ' is shown in Fig. 8, for a sparse array of square rings. As ω is reduced, T_f becomes lower, and the peak in χ' shifts to lower temperature. We can model the ac response of the rings with a straightforward extension of the theory of paramagnetic relaxation.[15,16] The susceptibility χ' as a function of frequency ω for an ensemble of *identical* noninteracting rings is

$$\chi'(T,H,\omega,\Gamma) = x_+\chi'_+ + x_-\chi'_- + \frac{(\mu_+-\mu_-)^2}{4k_BT}\,\frac{1}{(\omega/2\Gamma)^2+\left(\cosh\frac{F_+-F_-}{2k_BT}\right)^2}, \tag{4.2}$$

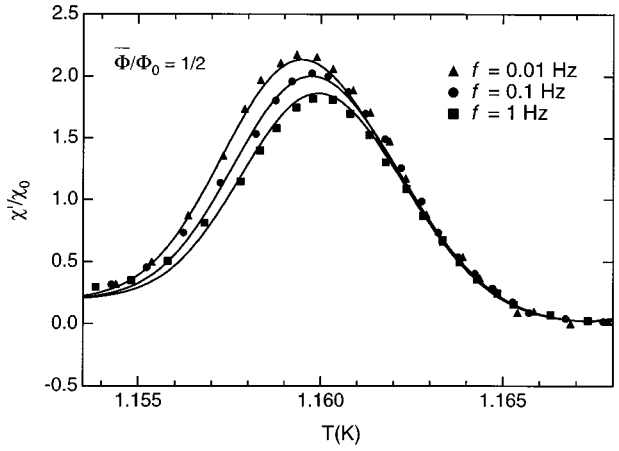

FIG. 8. Frequency dependence of the ac susceptibility at $\Phi_0/2$ for the noninteracting ''sparse'' array of square rings shown in the inset to Fig. 4. The solid lines are the fit described in the text.

where x_+ and x_- are the concentration of rings in the up and down spin states, and $F_\pm$, $\mu_\pm$, and $\chi'_\pm$ are the corresponding free energy, magnetic moment, and adiabatic susceptibility of those states. When $\omega=0$, the last term is the dc susceptibility derived from the statistical mechanics of one Ising spin.

Direct application of Eq. (4.2) does not fit the data in Fig. 8, because it gives a drop in χ' below T_f that is much more rapid than the observed behavior. However, intrinsic disorder in the arrays can give a distribution of flipping rates Γ. This will tend to broaden the peak. The lines in Fig. 8 were obtained fitting all the data in the figure simultaneously to a two parameter model that averages Eq. (4.2) over assumed Gaussian distributions in the rings' dimensions and coherence lengths:

$$\chi'(T,H,\omega) = \int\int d\xi(0)\,dL\,\chi'(T,H,\omega,\Gamma,\xi(0),L) \times \frac{1}{2\pi\delta\xi(0)\,\delta L} \times \exp\left[-\frac{(\xi(0)-\overline{\xi(0)})^2}{2(\delta\xi(0))^2}-\frac{(L-\overline{L})^2}{2(\delta L)^2}\right]. \tag{4.3}$$

Here, L is the average circumference of a ring, and hence the integral over L averages over the equivalent random field. The wire width was kept constant for simplicity. The value $\delta L/L = 0.5\delta A/A = 0.0027$ was fixed based on the rms variation in the ring areas $\delta A/A$ determined independently from the field scans of χ' described in the next section. The variation in flipping rate comes primarily from the distribution of coherence lengths in the rings, which presumably also arises from imperfections in the rings. Taking for $\overline{\xi(0)}$ the value given in Table I, the only free parameters left in the fit are $\delta\xi(0)$ and an overall scale factor. The fit gave $\delta\xi(0) = 0.03\xi(0)$.

The calculated frequency dependence of χ' is very sensitive to the energy barrier used to determine Γ. We found empirically that to obtain a good fit to $\chi'(\omega,T)$ it was nec-

essary to take $E_B \simeq |F|/3$. We propose an explanation for this value by noting that there is a possible intermediate state in which the order parameter goes to zero at one point on the ring circumference.[8] As such a state carries zero current, it is a plausible intermediate for a ring to pass through during the current reversal associated with a spin flip. For an infinitesimally thin ring, the free energy of this state is approximately 2/3 of the free energy of the spin states at $\Phi_0/2$, which means that $E_B \approx |F|/3$ as needed for the fit. The ratio of the energies of the intermediate state and the spin states is very weakly dependent on L/ξ, varying from 0.67 to 0.71 F for $\pi < L/\xi < 6$. Thus, we expect that approximately the same barrier is valid even for wide superconducting rings. It turns out that this state is a special case of the general saddle point states considered by Tarlie *et al.*,[17] and thus it is possible that this state does not represent the true barrier. A full exploration of the saddle point states is beyond the scope of the present analysis, but in light of the good agreement of the fit with the data, it is likely that this zero-current intermediate state is close to the true barrier.[18]

C. Field-dependent susceptibility

The magnetic measurements discussed in the previous sections demonstrate that individual rings are indeed analogous to Ising spins. However, those measurements do not tell us anything about the nature of possible *interactions* between the rings. To investigate this aspect of the problem, we have explored the *field dependence* of the magnetic susceptibility, $\chi(H)$. We find a broadening of the peak in $\chi(H)$, as well as a hysteretic behavior between field sweeps up and down. We show that both effects provide clear evidence of antiferromagnetic interactions between the rings.

Figure 9 shows the field dependence of χ for a *sparse* array of square rings. Since, as we have seen, the magnetic interactions between these sparsely spaced rings are about 18 times smaller than in dense arrays of rings, we expect that in these arrays interactions will be negligible. The upper graph shows field scans at temperatures higher than the peak in $\chi(T)$. At these temperatures we expect those rings that are near $H_{1/2}$ to flip freely with the ac field. The lower graph is obtained at temperatures below the peak temperature T_p. Here, rings are beginning to freeze out and we might expect slow dynamics and hysteresis to become important. The field was swept up (open symbols) and down (filled symbols). The lines between the points are fits to a Gaussian with a sloping background. The Gaussian shape in all the $\chi(H)$ curves comes from the distribution of the random fields, which again are related to the distribution in the rings' areas. Thus, at low applied fields, only those few rings with areas rather larger than the average size will feel an applied flux of $\Phi_0/2$ and thus be able to flip readily and hence contribute to the susceptibility. When the applied flux $\bar{\Phi} = \Phi_0/2$, then a large number of rings with areas equal to the average area can participate, leading to a peak in χ. Finally, for large applied fields, there is a contribution from only the few rather small rings. Thus the Gaussian shape of $\chi(H)$ directly reflects an evidently Gaussian distribution of ring areas, or, equivalently, of random fields. We have also added a sloping linear background to these fits to model the adiabatic limits of χ in the $n=0$ and $n=1$ states. From the data in Fig. 9, we

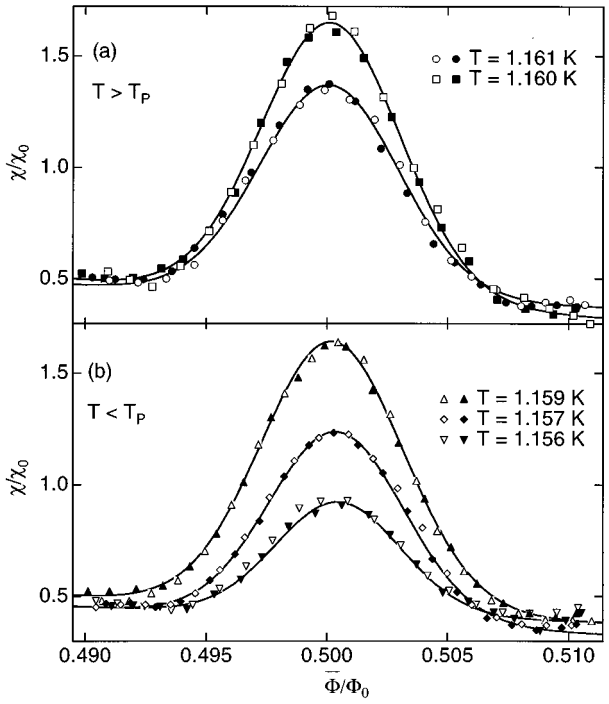

FIG. 9. Field-dependence of the ac susceptibility of noninteracting rings: χ' for a ''sparse'' array of square rings vs applied dc flux for fixed temperatures (a) above and (b) below the temperature T_p of the peak in $\chi(T)$. Open symbols: increasing field; filled symbols: decreasing field. Solid lines are fits to Gaussians plus a linear background. The widths of the Gaussians are independent of T, and reflect the distribution of the rings' areas and hence the random field.

find the standard deviation of the Gaussians for the sparse ring array to be $2.7\times10^{-3}\Phi_0 = 5.4\times10^{-3}\Phi_0/2$. Since $H_{1/2} = \Phi_0/2A$, this implies that the rms fluctuations in the ring areas is $\delta A_{\rm rms}/A = 0.0054$, or about half a percent.

In this treatment we have assumed that the *thermal* width of χ is small compared to this disorder-induced width. This is reasonable, since the width due to disorder is about eight times the thermal width, as can be calculated from Eq. (4.2), or obtained experimentally as described in Sec. V D. We also note that field sweeps up and down appear identical.

Field scans on arrays of closely spaced rings exhibit much more complex behavior than the sparse arrays, because of the inter-ring coupling. Figure 10 shows the effects of ring coupling on the susceptibility of a triangular lattice array. Again field sweeps up and down are shown, both above and below the temperature of the peak ($T_P = 1.172$ K). We note two important differences between this dense ring data and that from the sparse arrays (Fig. 9). First, the peak widths are wider for the dense array scans. Second, while above T_P the up and the down sweeps yield identical results, *below* T_P a splitting develops between the two sweep directions. Note that this splitting is such that the peak occurs *before* the applied flux is equal to $\Phi_0/2$ for the sweep up, but *after* $\Phi_0/2$ for the sweep down. We now show how these facts can be interpreted as evidence for antiferromagnetic interactions modified by dynamical freezing of rings.

Let us first discuss the broadening of the peak width. This effect is due to an average magnetic field generated by the

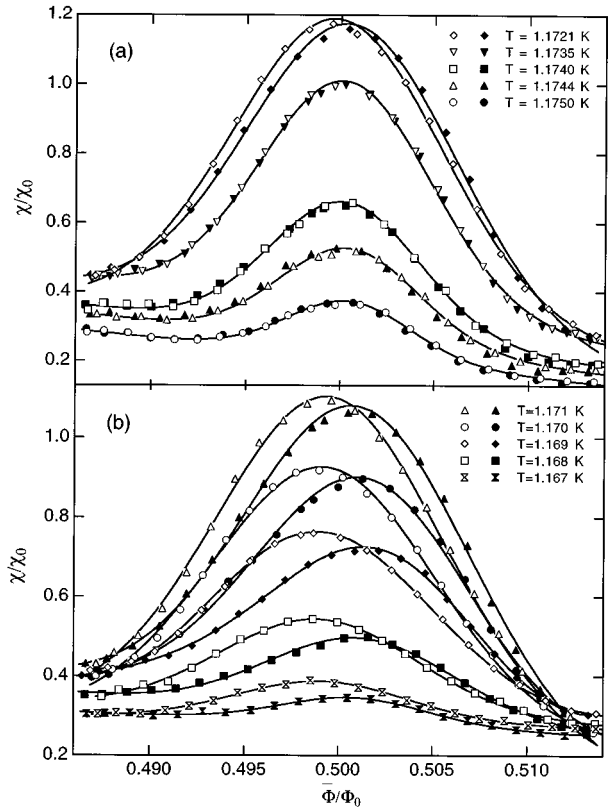

FIG. 10. Field-dependence of the ac susceptibility of interacting rings: χ' for a triangular lattice vs applied dc flux for fixed temperatures (a) above and (b) below the temperature T_p of the peak in $\chi(T)$. Open symbols: increasing field; filled symbols: decreasing field. Solid lines are fits to Gaussians. The temperature dependence of both the peak widths and the peak positions demonstrates the presence of interactions between the rings.

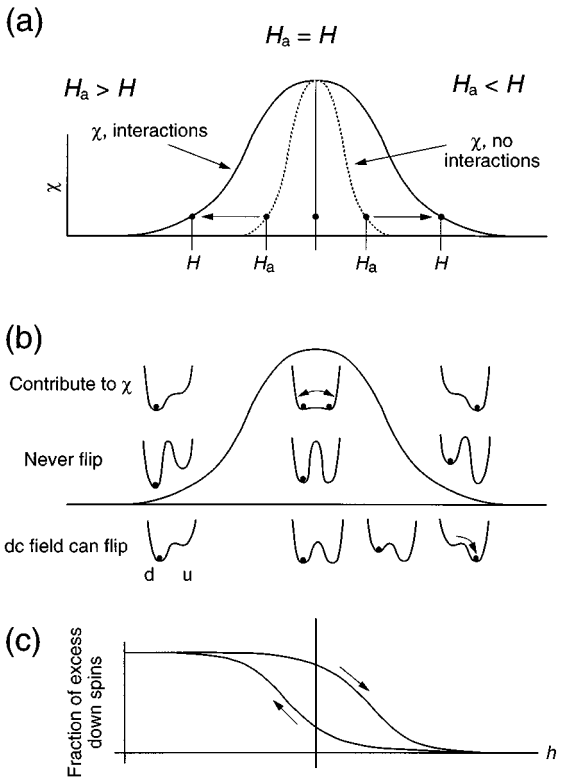

FIG. 11. (a) Broadening of the peak due to interactions. The dotted curve represents $\chi(H)$ for a noninteracting (i.e., sparse) array. Here the broadening is due to disorder only. In the interacting case, an applied field H below the peak is increased by the interaction field to an actual field H_a; the measured susceptibility is then $\chi(H_a)$, but it is *plotted* at H. As shown, this leads to an apparent broadening of the peak. A similar argument holds for applied fields above the peak. (b) There are three ''classes'' of spins: those with very small barriers at $H_{1/2}$, which flip freely at $H_{1/2}$ and contribute to χ; those with large barriers, which never flip at contribute nothing to the dynamics; and those with intermediate barriers, too large for the small ac field to flip, but which can flip once as the dc field ranges somewhat past their $H_{1/2}$. The excess number of such once-flipping spins is shown in (c). As the field is swept up, there is an excess of down spins, leading to an average upward mean field which persists well past the peak in χ. Upon sweeping down, however, there is a deficit of such spins, so that the mean field points up. This leads to hysteresis in $\chi(H)$ at lower temperatures where the ring dynamics begin to freeze out.

currents in the rings themselves. When we start a sweep at low fields, almost all the spins will point down. As we have seen, the dipolar nature of these downward-pointing moments leads to a magnetic field pointing *up* at neighboring rings. Thus, when all the rings point down, there is a rather uniform ''mean field'' pointing up. This means that the actual field H_a felt by the rings is *larger* than the applied field H [Fig. 11(a)]. The largest rings in the distribution will therefore reach their flipping field $H_{1/2}$ at a lower applied field than they would have without interactions, and the susceptibility will begin to rise sooner. This effect persists as long as there are more spins down than up, that is, until $\Phi=\Phi_0/2$. Here, there are as many up spins as down and the mean field is zero. As we move past $\Phi_0/2$, an excess of up spins develops, leading to a downward-pointing mean field. This means the actual field is somewhat *less* than the applied field, implying that the last few small rings will reach $H_{1/2}$ only at a larger applied field than would be the case with no interactions [Fig. 11(a)]. Thus the noninteracting Gaussian of Fig. 9 is spread out by interactions to the wider Gaussian of Fig. 10.

This explanation is adequate above the peak temperature T_P, where we expect the energy barrier for flipping to be small, and for each ring to contribute to the peak in χ when the applied field is near its $H_{1/2}$. However, we have seen that below T_P, a splitting develops between up and down sweeps. The above ideas cannot explain this, since in this picture the mean field is zero at $\Phi=\Phi_0/2$, and so the peak position should be the same for both sweep directions. To understand this splitting, we need to invoke the idea that below T_P, rings are beginning to freeze out. We have already seen (Sec. IV B) that there is a distribution of coherence lengths or, equivalently, of barrier heights. Thus, for $T<T_P$ we can think schematically of there being three ''classes'' of rings [Fig 11(b)]. Some rings will have barriers smaller than k_BT, and these can flip freely at $H_{1/2}$ and contribute to the peak in χ. Other rings will have very large barriers, and will never flip during the sweep. Some fraction, however, will have intermediate-sized barriers. These barri-

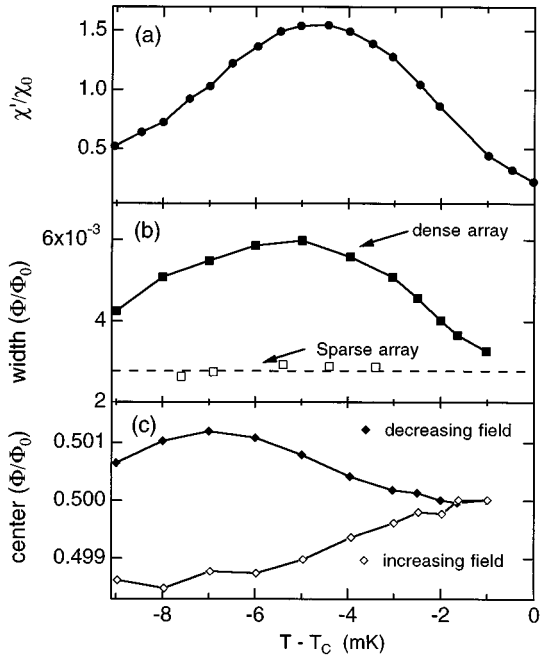

FIG. 12. Results of fits to field-dependent susceptibility of triangular lattice shown in Fig. 10. (a) ac susceptibility $\chi(T)$. (b) Width of peak. Also shown is width of peaks for sparse array from Fig. 9. (c) Splitting of peak.

ers are too large to allow the spins to follow the ac field, and they make no contribution to χ. However, they are small enough to allow the spin to flip from down to up after the applied dc field passes some distance beyond $H_{1/2}$. This is illustrated in Fig. 11(b). We see that such a spin starts in its down ''well,'' which is much lower than the up well at low applied fields. As the field is increased to this ring's $H_{1/2}$, the bottoms of the two wells become the same depth. However, the barrier is still large enough to prevent any flipping. Only when the dc field is somewhat *greater* than $H_{1/2}$ does the spin suddenly flip. Once it does so, however, it is now in the deeper ''up'' well, and cannot flip back. Given the distribution of barrier heights and ring areas, we expect then an excess of such down spins which persists past $\Phi_0/2$, as in Fig. 11(c). This implies a mean field pointing up, even at $\Phi_0/2$. This means the actual field is somewhat larger than the applied field, and the peak occurs before $\Phi_0/2$. When the field is swept back down, a similar argument holds, except there is now an excess of up spins which persists below $\Phi_0/2$. This moves the peak to a higher value of Φ on the downward sweep.

In Figs. 12(a)–12(c) we plot (a) the susceptibility $\chi(T)$, (b) the width of the peak, and (c) the peak splitting for the sweeps on the triangular array shown in Fig. 10. Shown for comparison in Fig. 12(b) is the peak width for the sparse square array data of Fig. 9. Note that the temperature scale is expanded to 8 mK. At high temperatures the peak width of the dense (interacting) array is similar to that of the sparse (noninteracting) array, but for the dense array the width begins to grow roughly linearly with falling temperature. The width of the sparse arrays is independent of T. These temperature dependences reflect the fact that the currents in the rings—and thus the interaction field caused by the rings—rises as $1-T/T_c$. Thus the peak width, which as we have seen is proportional to the interaction field, grows linearly with falling T. Of course, a sparse array has negligible interactions, and its width reflects only the disorder in the ring areas. A similar explanation holds for the initial rise of the peak splitting shown in Fig. 12(c). The splitting is proportional to the interaction field, which grows with falling T.

We note, however, that neither the peak width nor splitting continue to grow as the temperature is further lowered, and indeed both appear to begin to fall at the lowest temperatures in Fig. 12. This is because at these temperatures the energy barriers of all rings are rising rapidly. Thus, many rings are beginning to freeze out entirely, and never flip during the course of the sweep. The fraction of freely flipping spins, which determines the peak width, and of once-flipping spins, which determines the splitting, are both dropping.

To compare the strength of the random field to that of the interaction field, we may apply a quantitative analysis of the ideas shown schematically in Fig. 11. Let the field on a ring due to the current I flowing in one of its neighbors be $H_{\rm int}=MI/A$, with A the average ring area. Then we can compute the (mean) effective field h_a at a ring due to both the effective applied field h and the fields due to z nearest-neighbor rings as

$$h_a = h + zH_{\rm int}(x_- - x_+), \tag{4.4}$$

where x_+ and x_- are the concentration of up and down spins, respectively. If we assume a purely Gaussian distribution of ring sizes or flipping fields $H^i_{1/2}$ (as Fig. 9 implies), then x_+ is proportional to the area of the Gaussian which is *below* h_a. This is because all spins which have flipping fields below h_a will have flipped up, while all those above remain down. Thus we can write

$$x_+ = \frac{1}{\sqrt{2\pi}\sigma}\int_{-\infty}^{H_a} \exp(-y^2/2\sigma^2)\,dy = \frac{1+\mathrm{erf}(h_a/\sqrt{2}\sigma)}{2}. \tag{4.5}$$

Here, σ is the random Gaussian width (in field) determined from the noninteracting sparse array sweeps. Inserting this into Eq. (4.4) yields

$$h_a = h - zH_{\rm int}\ \mathrm{erf}(h_a/\sqrt{2}\sigma). \tag{4.6}$$

This equation yields $h_a(h)$ only implicitly. We can, however, expand this function around $h=0$, which yields

$$h_a = \frac{h}{1+z\sqrt{2/\pi}(H_{\rm int}/\sigma)} + O(h^3). \tag{4.7}$$

Thus to second order, the shape of the interacting-ring peak will be the *same* as that of the noninteracting peak, as seen in the data where Gaussian fits work well for both cases. The ratio of the widths of the peaks is then given by

$$R = \frac{\text{width of interacting peak}}{\sigma = \text{width of noninteracting peak}}$$

$$= 1 + z\sqrt{2/\pi}\,\frac{H_{\rm int}}{\sigma}$$

$$= 1 + z\sqrt{2/\pi}\,\frac{MI}{\sigma_\Phi}, \tag{4.8}$$

where σ_Φ is the random width measured in units of flux.

From Fig. 12 we see that at $T_c - T \approx 3$ mK the width of the interacting (dense array) peak is about $5\times10^{-3}\Phi_0$, while the width of the noninteracting (sparse array) peak is $\sigma_\Phi = 2.7\times10^{-3}\Phi_0$. Thus the ratio R is 1.9, yielding $MI = 0.19\sigma_\Phi = 1.05\times10^{-18}$ T m^2. With $M = 68$ fF for the hexagonal rings, we find that $I = 15\mu$A. Thus the rate of increase in current with falling temperature is about $dI/dT = 15\ \mu$A/3 mK$=5$ mA/K.

We may compare this with the currents per ring derived directly from magnetization measurements. The best estimate of the moment of one ring near $\Phi_0/2$ can be found from the data of Fig. 6, in which the arrays were zero-field cooled and then had the field turned on. The low $T^\star = 1.1578$ K data yields a slope $d\mu/dT = 1.3\times10^{-11}$ emu/K. We may convert from moment to current using Eqs. (A10) and (A13), computing $\mu = I\widetilde{K}(0,H)/c\widetilde{J}(0,H)$. The ratio $\widetilde{K}(0,H)/\widetilde{J}(0,H)$ thus plays the role of an effective ring area for the $n=0$ state, and can be computed from Table I. For the hexagonal rings, $\widetilde{K}(0,H)/\widetilde{J}(0,H) = 3\sqrt{3}(b^2+a^2)/4 = 1.68\times10^{-12}$ m^2. We find that dI/dT computed this way is 7.7 mA/K, which agrees quite well with the 5 mA/K found from the previous method. The broadening of the susceptibility peaks in the dense (interacting) arrays is thus seen *quantitatively* to be caused by the dipolar interactions between rings.

V. MAGNETIC IMAGING

The magnetic measurements—magnetization and susceptibility—presented in the previous section have established first, that individual rings in the arrays behave analogously to spins in a random-field Ising model; and second, that there are magnetic interactions between rings which favor antiparallel alignment, that is, that there exists an *antiferromagnetic* coupling between the rings. The magnetic measurements could not determine, however, whether short- or long-range order in the spin orientations exists in the arrays. To answer this question, we have used scanning Hall probe microscopy to image directly specific ''spin'' configurations in the arrays. We can then analyze these real-space configurations to explore the degree of spin-spin correlations present.

Field-cooled images of the ring arrays were taken with the scanning Hall probe microscope (SHM) at low temperatures ($T \approx 0.5T_c$), where the currents flowing in each ring are large enough to be measured by the Hall probe. An external magnetic field was applied to the array by a home-built superconducting magnet which was used in the persistent mode. This way the field was very stable and the magnetic noise was very small. The field nonuniformity over the entire area of the array was about one part in 10^4, which is much smaller than any other field scale in the measurements. At each value of the applied field, the rings were cooled through T_c at typical cooling rates of 30–50 mK/s. However, cooling through the transition region at the much slower rate of 0.017 mK/s had no effect on the resulting correlations. Since as we have seen, the ring dynamics freeze out only some 10 mK below T_c, the images we obtained are essentially snapshots of the configurations at the freezeout temperature. Also, at the scan temperature of ≈ 0.6 K, the flux configuration is frozen in, so that the Hall probe was noninvasive during the scans. The measuring current of 50 μA through the Hall probe results in a maximum field at the rings of about 0.16 G, which is completely negligible at low temperatures. A typical scan covered an area equal to $48\times62\ \mu$m^2, and took five minutes to perform. The data were stored as 128×128 pixel raster scans.

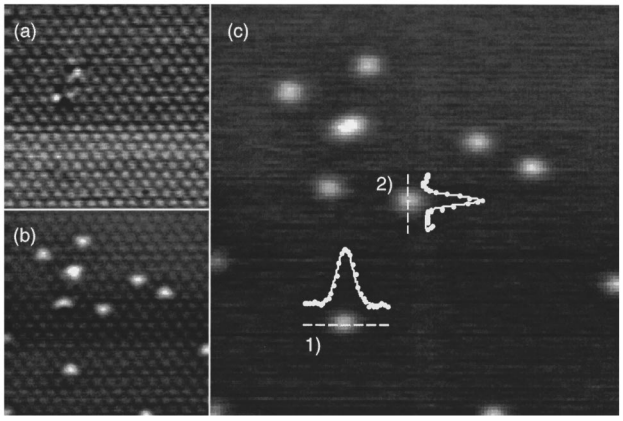

FIG. 13. (a) Magnetic image of a honeycomb lattice in an applied flux of 0.436 Φ_0; here, all the rings are in the spin down state. The triangular lattice of bright spots shows the lattice holes, i.e., the positions of the missing rings in the honeycomb lattice. (b) Image obtained at 0.4913 Φ_0 in the same region of the array. The few triangular-shaped bright spots are rings containing a single flux quantum, that is, they are ''up spins.'' (c) The difference between the two images. Here, the up spins are quite obvious as roughly elliptical white spots. Also shown are field profiles through two spins in both horizontal (1) and vertical (2) directions. The circles are the field values, and the curves are Gaussian fits to the field profiles. The amplitude of the Gaussians is 0.53 G.

A. Image reconstruction

To compute accurate statistical measures of the correlations, we need to be able to determine the correct orientation of each magnetic spin in the array. Figure 13(a) shows the magnetic field distribution over a honeycomb lattice field cooled in 6.1 G, which is equal to an applied flux of 0.436 Φ_0. The X and Y axes are the voltages applied to the scanner, which are nominally proportional to the x and y positions. The image was obtained by scanning from left to right in lines from top to bottom. The full scale field modulation in Fig. 13(a) is 0.1 G. Brighter regions of the image correspond to regions of higher field. The distortion of the measured pattern on the left side is caused by hysteresis in the piezoelectric scanner. Because the voltage responses of the scanner in the X and Y directions are not the same, the distance scanned in the Y direction is about 1.4 times that scanned in the X direction. This far below $\Phi_0/2$, all the rings cooled in the $n=0$ state. We immediately notice a triangular array of bright spots. These appear at the position of the empty spaces (holes) in the honeycomb lattice, which form a triangular lattice. Since the rings screen out the applied magnetic field, the field is pushed into the holes, and the field through the holes is greater than the applied field. Figure 13(b) shows the

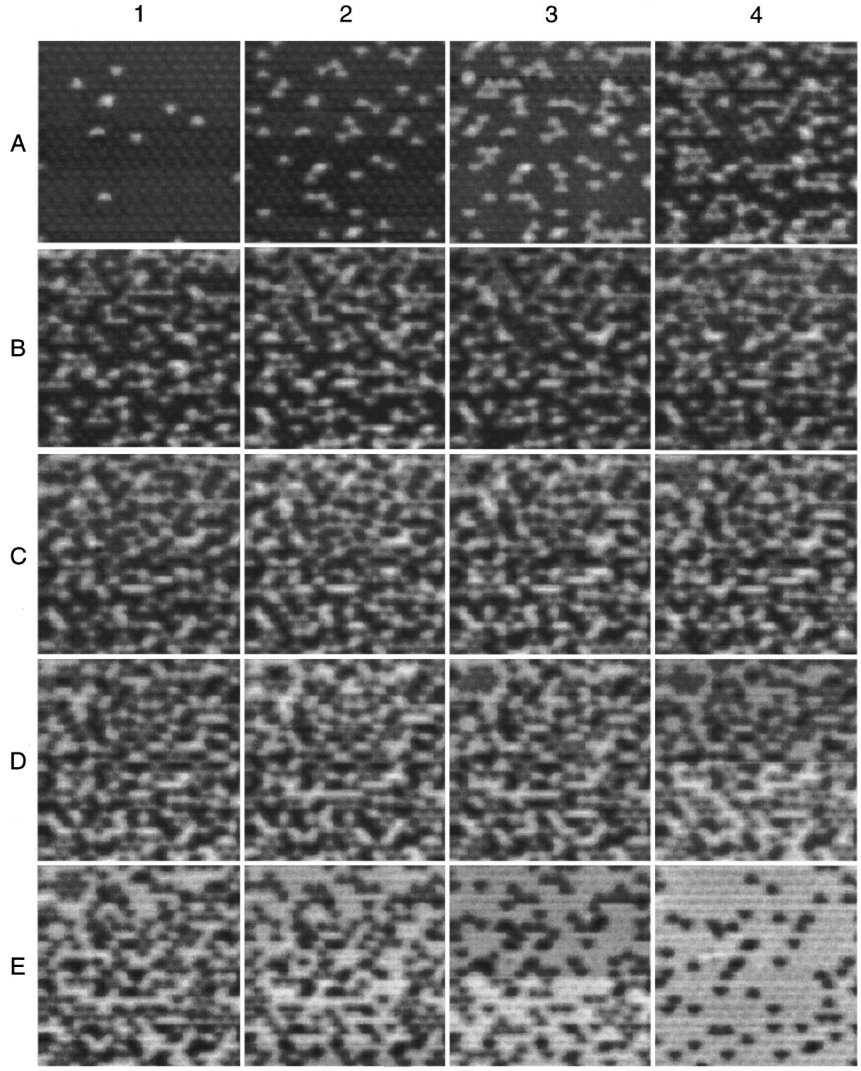

FIG. 14. A sequence of field-cooled images of the honeycomb lattice, taken in increasing applied fluxes near $\Phi_0/2$. The flux increases from left to right starting at the upper left corner where $\Phi = 0.4913\Phi_0$ and ending in the lower right corner at $\Phi = 0.5066\Phi_0$. There is a clear progression from a few up spins (white spots) at low fields, through rather disordered-appearing states near Φ_0, to only a few down spins (dark spots) at the highest applied fields.

field distribution at a somewhat higher field corresponding to $0.4913\ \Phi_0$. Here, a few rings in the array cooled in the spin up state. Those rings appear as large bright spots. The superposition of the field from the up spin with the field from the three neighboring holes causes the spots to have a triangular shape. The full-scale field here is 0.42 G.

The positions of the underlying rings can be obtained from Fig. 13(a) by finding the center of every bright spot (hole) in the image. These determine the ring locations, since on a honeycomb lattice, the rings lie at the center of the equilateral triangle formed by the three neighboring holes. The image contains 680 rings. The SHM is sufficiently stable that the ring positions determined in this way can be used to analyze a series of images of the same portion of the array taken at different fields.

The difference image formed by subtracting Fig. 13(a) from Fig. 13(b) is shown in Fig. 13(c). The triangular lattice of holes is absent in the difference image, and the remaining bright spots are the magnetic field produced by the up spins. The full scale magnetic field modulation in this image is 0.53 G. The measured field profile of a single ring is well-described empirically by a 2D Gaussian. This profile is illustrated in two plots along lines 1 and 2 in Fig. 13(c); also shown are the Gaussian fits to these two slices. Note that the width of the Gaussians along the X and Y directions are different by the factor of 1.4 mentioned previously.

Figure 14 shows a set of 20 images of the honeycomb lattice, obtained in different fields around $\Phi_0/2$ spanning the range $0.4913\ \Phi_0$ to $0.5066\ \Phi_0$. At low fields, only a few up spins (bright spots) are visible on the dark background of down spins, and the faint lattice of holes. At larger fields, the number of up spins increases until at the highest fields most of the rings are spin up, with only a few dark down spins. In this case, the hole lattice appears as a regular array of gray spots. To determine the spin state of each ring, we developed the following image reconstruction algorithm. First, we make an initial guess at the correct spin configuration. When there are only few up spins as for the smallest field in Fig. 14, the spin configuration is straightforward to determine. Near $\Phi_0/2$, the initial guess was the spin configuration determined at the previous field. After the initial guess, we construct a corresponding *synthetic image* by the superposition of computer-generated Gaussian field profiles of the appropriate sign at each site. The difference image of data minus model is computed, and used to determine how to modify any incorrectly chosen spins. These steps are iterated until the difference image is flat. This procedure is illustrated in Fig. 15. The top left image is the measured magnetic field distribu-

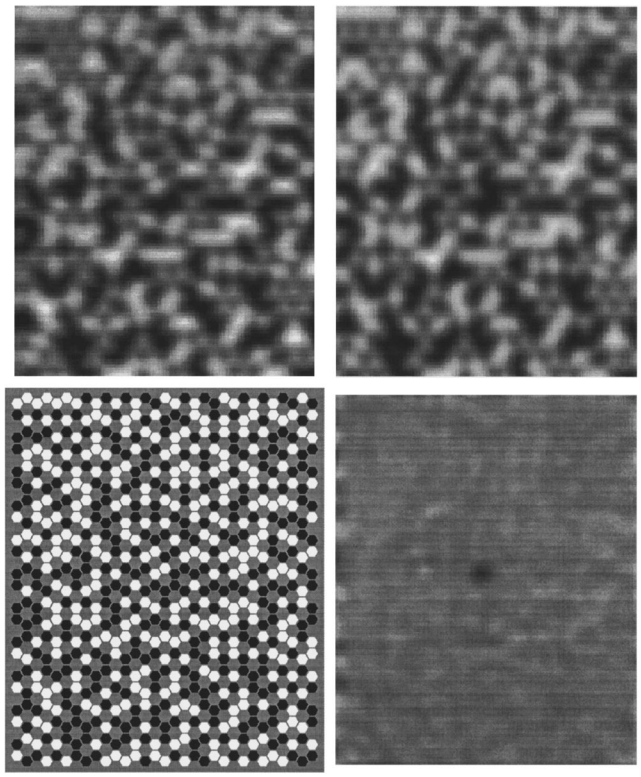

FIG. 15. Top left: A magnetic image measured at $\Phi_0/2$ for a honeycomb lattice. Top right: The synthetic image which models the data, as described in the text. Bottom left: The spin configuration inferred from the data. Dark hexagons represent down spins, and bright hexagons up spins; gray hexagons are the holes of the honeycomb lattice. Bottom right: The difference between the synthetic and the measured images. We have purposely set one spin incorrectly in the synthetic image; this error shows up very clearly in the difference image as an isolated dark spot.

tion C4 of Fig. 14 stretched along the vertical axis to correct for the anisotropy of the scanner. The top right image is the final synthetic image, and the computed spin configuration is shown at the bottom left. Dark hexagons are down spins and white hexagons are up spins. The difference between the synthetic image and the measured image is shown at the bottom right. To demonstrate the effectiveness of our modeling procedure, one spin was deliberately set incorrectly in the synthetic image; this error shows up very clearly in the difference image.

A similar image reconstruction algorithm was used in the analysis of the kagomé lattice. However, the triangular and the square lattice do not have holes, and the ring positions were determined using a different method. First, we note that images taken at two nearby fields are very similar, and the difference image of two such images typically shows only a small number of flipped rings. In Fig. 16 we show two images of a triangular lattice taken at $H=7.000$ and 7.013 G. The corresponding difference image shows both bright and dark spots, indicating that some rings flipped from down to up, and some from up to down. The positions of these spots determine the locations of the flipped rings. This procedure was repeated for the difference images from a series of images taken at fields that span $\Phi_0/2$. In such a series every ring flips at least once, as can be seen for the honeycomb

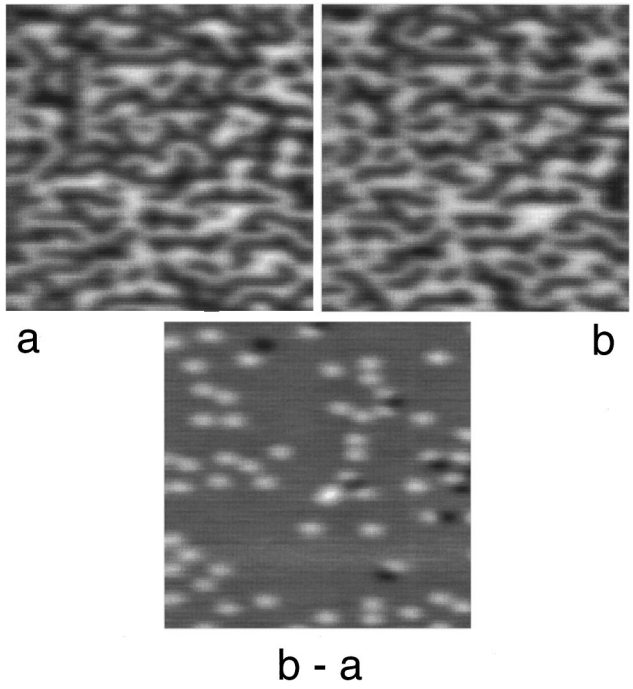

FIG. 16. Magnetic images of a triangular lattice at $H=7$ G (a) and $H=7.013$ G (b). The difference image (b)–(a) is shown below. Bright spots in difference image are rings that flipped up and dark spots are rings that flipped down between these two field-cooled images. The spot positions accurately define the positions of the rings.

lattice in Fig. 14, and the positions of all the rings can be found. Once these positions are known, the previously described image reconstruction algorithm may be applied.

B. Analysis of the spin configurations

Figures 17 and 18 show the magnetic field images and corresponding spin configurations at five different fields near $\Phi_0/2$, for the honeycomb, kagomé, triangular, and square lattices. Again, the magnetic images have been stretched along the vertical axis to correct for the anisotropy of the piezoelectric scanner. As the field increases the concentration of up spins increases. At $\Phi_0/2$, by definition the fraction of up spins in the array is the same as the fraction of down spins. At the highest field, the down spins appear as a few dark spots. Each lattice was scanned over two different regions of the array. In these two figures we show the field scans over one area for each lattice only.

Figure 19 shows the concentration of up spins x_+ for all the arrays, as a function of magnetic field. x_+ was determined by simply counting the number of up spins in each image. The data for the honeycomb lattice was obtained from the images in Fig. 14. The lines are fits to an error function, i.e., to the integral of a Gaussian. The Gaussian widths in Fig. 19 are shown in Table II. As explained in Sec. IV C, the widths are larger for higher coordination numbers due to the larger average interaction field. That these curves are well fit by an integral of a Gaussian again reflects the Gaussian distribution of ring sizes as described in Sec. IV C. Only a few very large rings will point up at applied average fluxes well below $\Phi_0/2$, and only a few small ones will still be down at fluxes well above $\Phi_0/2$.

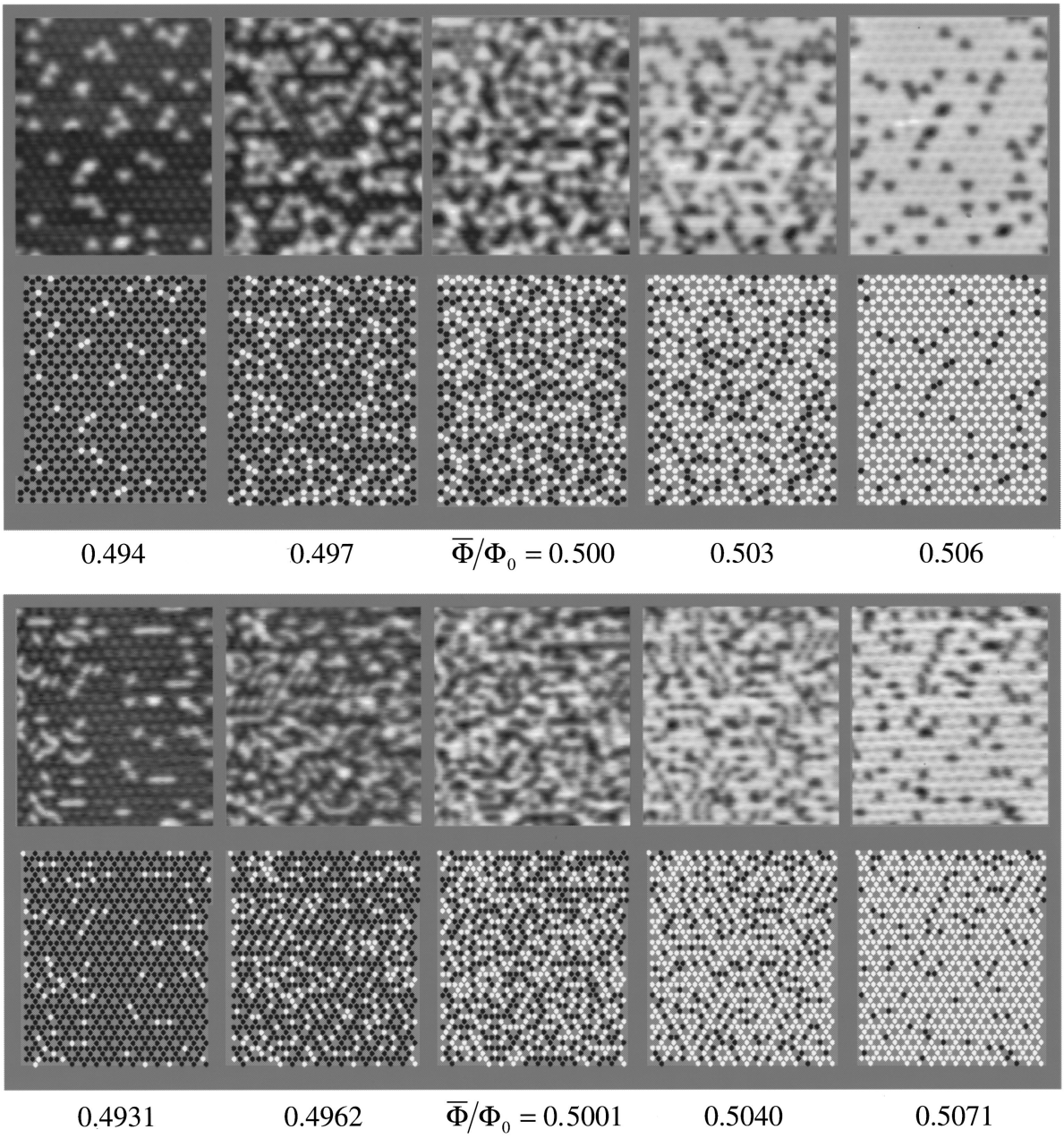

FIG. 17. The magnetic field above the arrays for the honeycomb and kagomé lattices, at several increasing applied fluxes. Up spins again appear here as white spots, and down spins as black ones. The spin configurations as deduced from the images are shown under each image. Here, white hexagons represent up spins, and black hexagons down ones. Gray hexagons represent the holes of each lattice.

The field-cooled images corresponding to successive fields in Fig. 19 appeared very similar, and the difference images show that only a very small fraction of spins change from point to point. Figure 20 shows the difference between the images at 0.5006 Φ_0 and 0.5 Φ_0 on the honeycomb lattice (panels D2 and C4 in Fig. 14). The field change between these two images (8 mG) is close to the rms amplitude of the ac field (6 mG) that was used in the susceptibility measurements in Sec. IV. We see that most of the rings cooled down in the same spin state, and only 50 out of 680 actually changed. Of these, 35 changed from down to up, and 15 changed from up to down, resulting in a net gain of 20 spins up. Since not all the rings that changed flipped from down to up, evidently the field increment is smaller than the thermal width of the spin distribution function. By thermal width we mean the width that the $x_+(H)$ curve would have for an array of perfectly identical rings. Hence, the ac susceptibility measurements in Sec. IV were done in the regime where $\mu H_{\rm ac} < k_B T$; we have already seen that the response was linear with ac field. The thermal width will be discussed in more detail in the next section. Because the great majority of the rings did not change between the two fields, this means that the width of the distribution function in Fig. 19 comes mostly from the disorder, i.e., from the random field.

The reconstructed ring configurations shown in Figs. 17 and 18 show that there are no long-range correlations in the arrays. Indeed, at first glance the distribution of spins appears random. However, the appearance of a *truly* random configu-

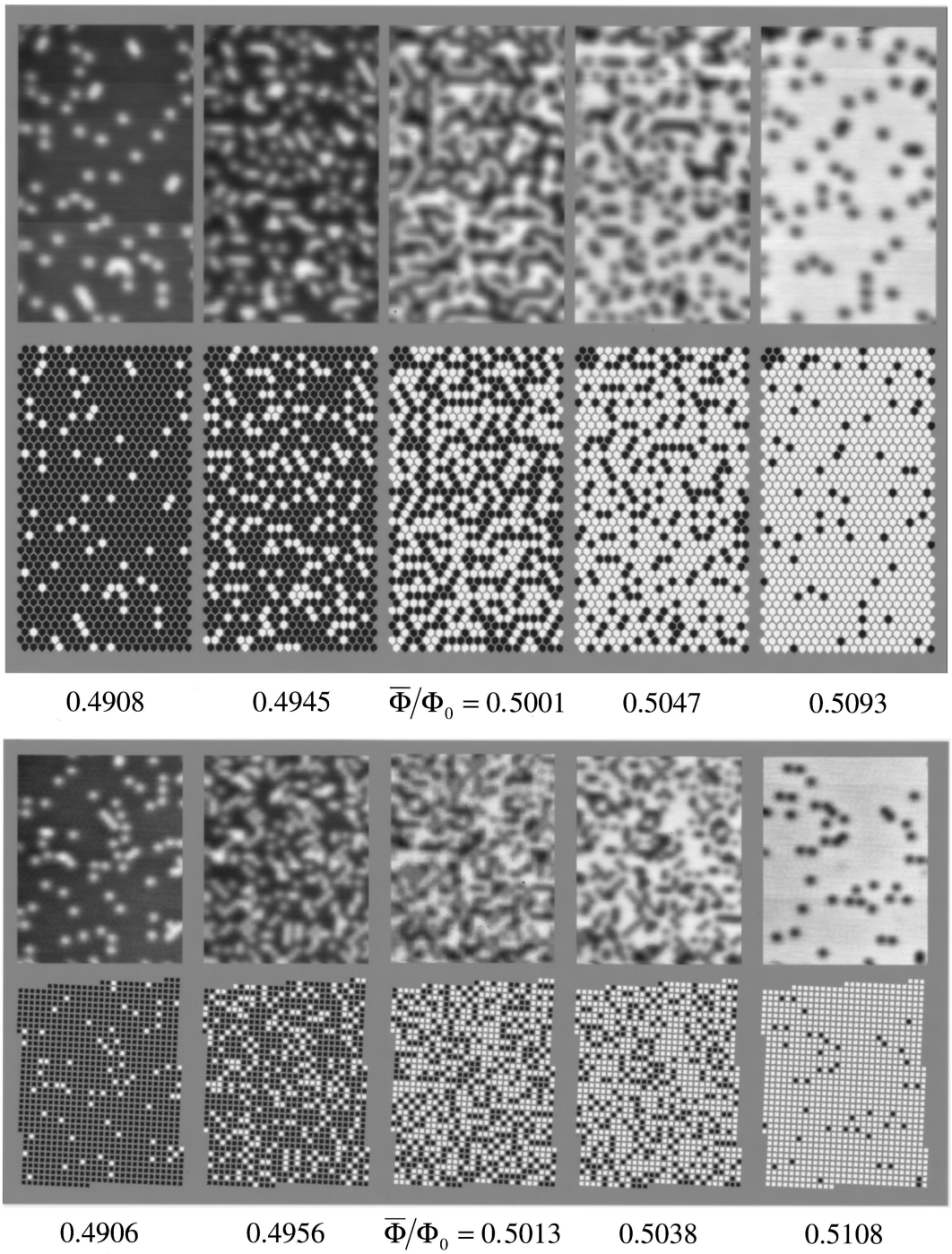

FIG. 18. The magnetic field above the triangular and square lattices; see Fig. 17 for details.

ration is noticeably different. In Fig. 21(a) we show a real magnetic image (the same shown in Fig. 15), and in Figs. 21(b)–21(d) we show three synthetic images generated using completely random spin configurations, but at the same value of x_+. The difference between the three random images and the real image is clear: the random configurations have rather large ''ferromagnetic'' patches of up spins (light areas) and down spins (dark areas), due simply to the statistics of a

TABLE II. Gaussian widths of the distribution of fields for $\Phi_0/2$ and the bond order parameter for the ring arrays.

	Honeycomb	Kagomé	Triangular	Square
width (G)	0.0697	0.0754	0.1018	0.1031
$\sigma(H_{1/2})$	-0.18 ± 0.02	-0.15 ± 0.02	-0.15 ± 0.02	-0.18 ± 0.02

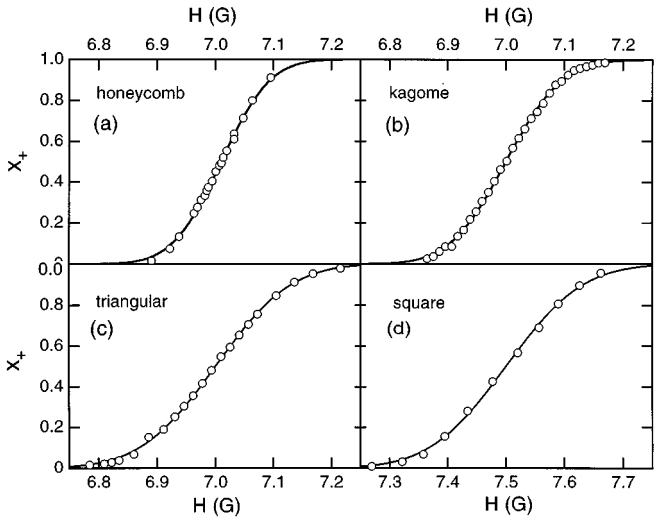

FIG. 19. Up spin concentration x_+ vs field for the ring arrays. Each data point corresponds to a field-cooled image; the data in (a) are from the images in Fig. 14. Solid lines are Gaussian fits as described in text; the resulting widths are given in Table II.

random configuration. The real data, however, lacks such large areas of parallel spins, and has a much ''finer-grained'' appearance. This is due to the presence of short-range antiferromagnetic correlations which favor antiparallel alignments of neighboring spins.

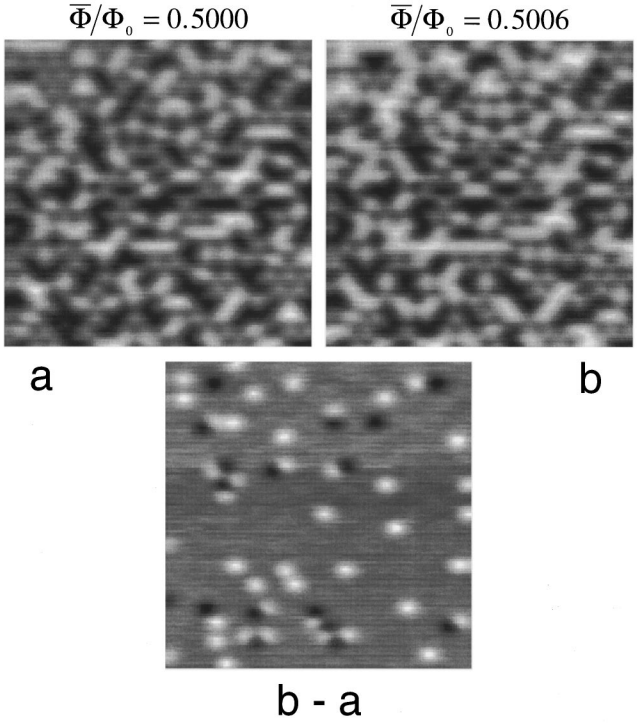

FIG. 20. Images in an applied flux of 0.5000 Φ_0 (a) and 0.5006 Φ_0 (b), and their difference image. Most of the spins in the two images are the same, resulting in a gray color in the difference image. Spins which flipped from down to up appear as white spots in the difference; those which flipped from up to down as dark spots. Because the external field was increased between these two images, most of the spins which flipped up. However, a few flipped down due to thermal fluctuations.

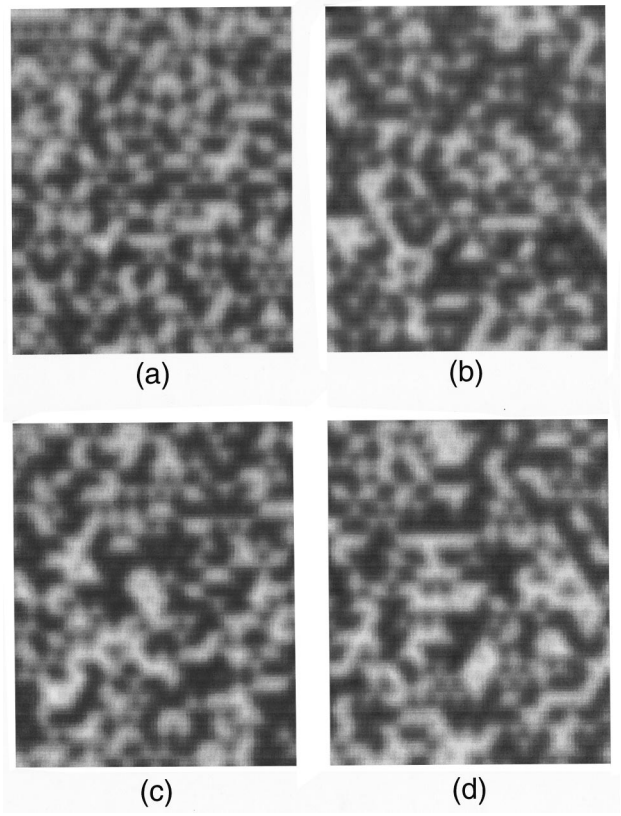

FIG. 21. (a) A magnetic image of the honeycomb lattice (the same as C4 of Fig. 14). Also shown [(b)–(d)] are three synthetic images constructed from completely random data with the same fraction of up spins as (a). They are characterized by noticeably larger regions of adjacent up spins and adjacent down spins than the real data in (a). The spins in (a) have correlations which favor antiparallel orientations of spins, and discourage the growth of any large ferromagnetic patches.

To quantify these considerations, we measure the correlations in this disordered system using the the near-neighbor *bond order parameter*.[19,20] It is defined as

$$\sigma = 1 - \frac{x_{\mathrm{AF}}}{2x_+x_-} = 1 - \frac{x_{\mathrm{AF}}}{x_{\mathrm{AF}}^{\mathrm{rand}}}, \tag{5.1}$$

where x_+ and x_- are the fractions of up and down spins, and x_{AF} is the fraction of antiferromagnetic near-neighbor *bonds*, that is, bonds between an up spin and a down spin. For a completely random spin distribution, $x_{\mathrm{AF}} = x_{\mathrm{AF}}^{\mathrm{rand}} = 2x_+x_-$, which gives the second form of Eq. (5.1). It is clear from this definition that for a completely random configuration of spins $\sigma = 0$. If there is an excess of ferromagnetic bonds (over the random case) then $\sigma > 0$, and if there is an excess of antiferromagnetic bonds then $\sigma < 0$. Indeed, when $\sigma < 0$ one can interpret the magnitude of the order parameter as the excess fraction of AFM bonds as compared with the purely random case. The bond order parameter is related to the nearest-neighbor spin-spin correlation function as $\langle s_i s_j \rangle - \langle s_i \rangle \langle s_j \rangle = 4\sigma x_+ x_-$, where s_i and s_j are Ising spins on sites i and j, respectively. The averaging here is over the spins in the arrays.

At any value of x_+, there is a most-negative possible value of σ, which ranges from $\sigma = 0$ when $x_+ = 0$ or 1 to

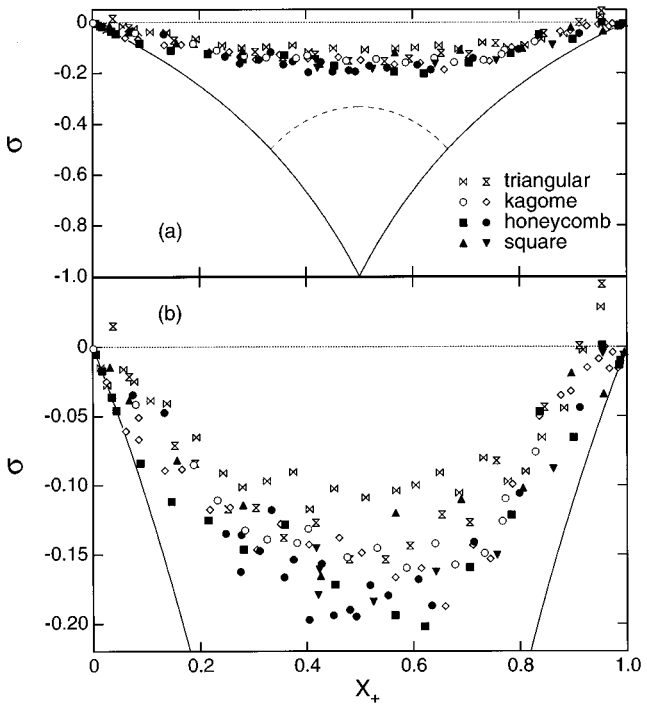

FIG. 22. (a) Bond order parameter σ vs up spin concentration x_+ near $\Phi_0/2$. $\sigma<0$ for all arrays, indicating AFM correlations. Solid lines are maximally negative possible values of σ for bipartite lattices. Frustrated lattices have an additional constraint indicated by the dashed line. (b) Expanded view of data showing greater AFM correlations for bipartite honeycomb and square lattices than for frustrated triangular and kagomé lattices.

$\sigma=-1$ when $x_+=0.5$, for bipartite geometries such as the square lattice. This is because (for $x_+<0.5$) the most antiferromagnetic possible case is when each up spin is surrounded by down spins, i.e., the up spins never abut. Thus $x_{\rm AF}^{\rm best}=2x_+$. The most-negative value of σ, $\sigma_{\rm min}$, will occur in this case. As we have seen, $x_{\rm AF}^{\rm rand}=2x_+x_-$, so that $\sigma_{\rm min}=1-x_{\rm AF}^{\rm best}/x_{\rm AF}^{\rm rand}=x_+/(x_+-1)$. In the bipartite lattices it is in fact always possible when $x_+<0.5$ to arrange the up spins so that they do not abut, and so it is theoretically possible for σ to reach $\sigma_{\rm min}$. This minimum value of σ is shown as the solid line in Fig. 22(a). In general, however, because of disorder and thermal fluctuations, σ will lie above this lower bound.

For the frustrated triangular and kagomé lattices, geometrical constraints do not allow up spins to avoid each other all the way up to $x_+=0.5$. At $x_+=1/3$, it becomes impossible to place one more up spin such that it does not abut another up spin. The best one can do is to keep $x_{\rm AF}^{\rm best}$ constant in the range $1/3<x_+<2/3$. This leads to a small hump in the $\sigma_{\rm min}$ vs x_+ curve, as shown by the dashed line in Fig. 22(a). One would then expect to see strong differences in σ between the bipartite and frustrated lattices whenever σ approached this part of the diagram.

For each image and its equivalent spin configuration we calculate both x_+ and σ, from simple counting of spins and bonds, and using the definition in Eq. (5.1). We then plot σ as a function of x_+. The results for each of two different areas of all the lattices are shown in Fig. 22. The values of σ for all lattices are well above $\sigma_{\rm min}$, but are nonetheless clearly negative within the scatter over the entire range of x_+. The fact that σ is negative means that the spins are correlated antiferromagnetically. The values of σ near $\Phi_0/2$ on the various lattices are summarized in Table II. That σ is far from $\sigma_{\rm min}$ is due mostly to the effects of the random field; as we show in Sec. V D, the effects of thermal fluctuations are relatively small.

To obtain the uncertainty $\delta\sigma$ of the bond order parameter, we first note that for each data set in Fig. 22, consecutive values of σ are not statistically independent because they come from images taken in the same part of the array, and hence all have the same realization of the random field. Since we scanned at only two different parts of each lattice, we have only two realizations of the random field. There will be differences in σ as measured in different areas of the array due simply to the finite number of spins in one area. Thus we calculated the fluctuation $\delta\sigma$ by averaging σ over many computer-simulated realizations of the random field on 680 spins (with no interactions). The standard deviation was found to be $\delta\sigma=0.03$. Since we have two realizations of the random field, $\delta\sigma\approx 0.03/\sqrt{2}\approx 0.02$. We also measured the next-near-neighbor bond order parameter for each array, and find that it is consistent with zero. Therefore, the correlations are short range only.

Since the honeycomb, kagomé, and triangular ring arrays were made of the same kind of rings with the same near-neighbor spacing, the only difference between them is the lattice geometry. Therefore, we can compare the bond parameter for these lattices directly. Although there is some scatter, Fig. 22 indicates that the bond order parameter on the bipartite honeycomb lattice is more negative than the order parameter on the triangular and kagomé lattices, which are nonbipartite. (Additionally, near $\Phi_0/2$, σ is approximately the same on the bipartite honeycomb and square lattices.) This is direct evidence for a suppression in the ordering due only to effects of geometrical frustration. We note, however [Fig. 22(a)], that disorder evidently prevents $\sigma(\Phi_0/2)$ from coming particularly close to $\sigma_{\rm min}$ in any case. Only when the bipartite lattices approach the frustrated-lattice value of $\sigma_{\rm min}(\Phi_0/2)=-1/3$ would we expect there to be very strong differences between the lattices.

C. Higher fractions of Φ_0

In addition to the applied flux equal to $\Phi_0/2$, we measured the spin configurations at higher flux fractions $\nu=3/2$, 5/2, 7/2, and 9/2. At higher fractions, the region of fields where we see both up spins and down spins is wider. The concentration of up spins as a function of field at higher fluxoid states is shown in Fig. 23 for the honeycomb (a) and kagomé (b) lattices. The lines between the points are fits to error functions. The widths w determined from these fits are shown in the insets. The widths as a function of field appear to be a linear function of fraction ν. This is because the random field is caused by the differences in the ring areas, and grows with ν. The field for ν flux quanta in a ring with area A is equal to $H_\nu=\nu\Phi_0/A$. If the spread of the areas in the array is δA, and if it is small, then we can estimate the spread in fields δH_ν: $\delta H_\nu=\nu\Phi_0\delta A/A^2$.

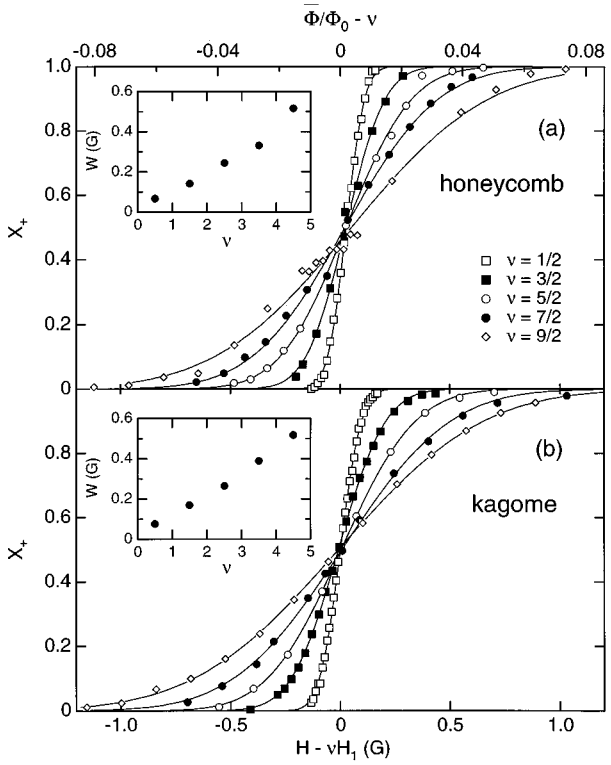

FIG. 23. Up spin concentration x_+ vs field at different flux fractions ν for the honeycomb (a) and kagomé (b) lattices. Data for different fractions have been shifted to permit direct comparison of widths of $x_+(H)$ distributions. Insets show widths determined from Gaussian fits (solid lines).

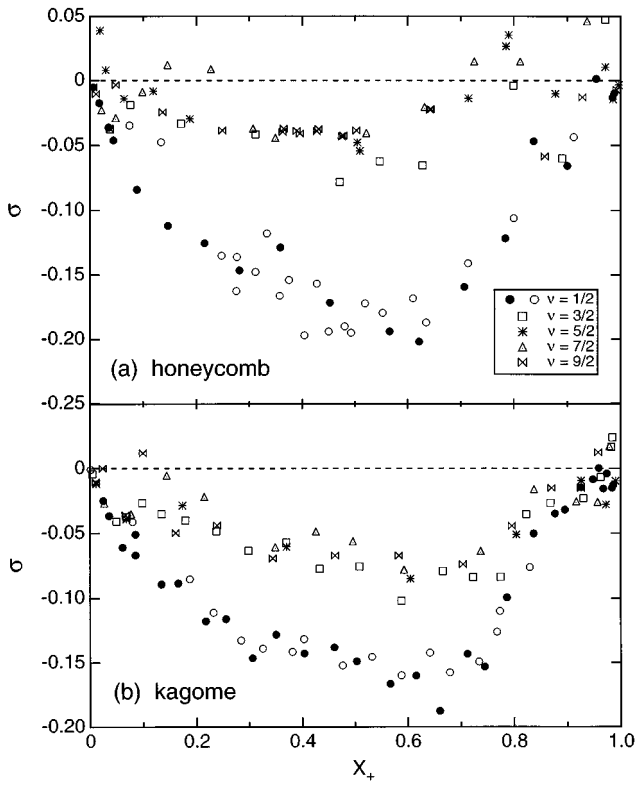

FIG. 24. Bond order parameter σ vs up spin concentration x_+ at different flux fractions ν for the honeycomb (a) and kagomé (b) lattices. σ is reduced with increasing ν indicating increasing effective disorder.

Therefore, the widths of the Gaussian distributions are linear with the fraction number. Since the interaction between the rings does not grow with field, one expects to see a reduction in the short-range correlation function at higher fractions. Indeed, Fig. 24 shows that σ at higher fractions is much smaller than σ at $\Phi_0/2$. The disorder in the ring arrays is therefore a tunable parameter.

D. Repetitive cooling experiments

The distribution function of up-spin concentration vs field that is shown in Figs. 19 and 23 originates from three effects: (1) the random field that comes from the distribution of ring areas around the average area, (2) the ring-ring coupling, which has the tendency to widen the Gaussian distribution as shown in Sec. IV B, and (3) thermal fluctuations. In this Section, we analyze the statistics of repeated cooldowns at $\bar{\Phi}=\Phi_0/2$ to estimate the thermal width relative to the combined effects of the disorder and the interactions.

The ac susceptibility measurements in Sec. IV B showed that the freezing temperature T_f is very weakly frequency dependent. In this analysis we will assume that the dynamic freezing occurs suddenly at T_f, and that the rings are in equilibrium above T_f. In this case, the spin configurations measured with the SHM reflect the Boltzmann distribution function at T_f, and the probability that a ring will cool into its spin up state is

$$p_+=\frac{1}{1+e^{(F_+-F_-)/k_BT_f}}, \tag{5.2}$$

where

$$F_+-F_-=2\sum_j V_{ij}s_j-(\mu_+-\mu_-)(h+h_i^r) \tag{5.3}$$

from Eq. (2.2).

Figure 25 shows images of 2 of 20 cooldowns taken in one region of a honeycomb lattice array at $\bar{\Phi}=0.5005\Phi_0$. The difference image is shown below. The dark spots in the difference image are rings that flipped from up to down between cooldowns, and the bright spots are rings that flipped from down to up. Most rings cool down in the same state every time; in the twenty repetitions that were done, 75% of the 653 rings in the imaged area always cooled in the same state, that is, had $p_+=0$ or 1. Other values of p_+ were less common; by counting the number of times each ring cooled into the spin-up state we may construct a histogram of the fraction $F(p_+)$ of rings that had probability p_+ for being spin up. This is shown in Fig. 26, where we again note the large values of F at $p_+=0$ and $p_+=1$. We find there are interesting spatial correlations between rings which tend to flip more often. To illustrate this, we plot in Fig. 27(a) a grayscale map of the probability $P_f=2p_+(1-p_+)$ that each ring changed its state between any two cooldowns. Dark gray corresponds to $P_f=0$, i.e., to rings that never change state, and white corresponds to $P_f=0.5$, that is, to rings which flip quite readily above T_f. The gray levels in between represent the intermediate probabilities.

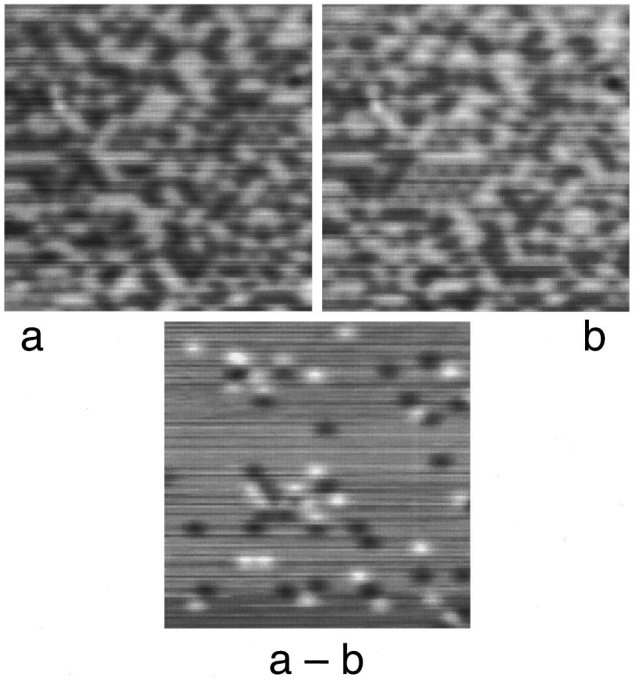

FIG. 25. (a), (b): Two magnetic images of the honeycomb lattice, obtained after cooldowns in the same applied flux $\Phi = 0.5005\Phi_0$. The differences between these images is shown below. Thermal fluctuations cause some spins to change their orientation between successive cooldowns, although the majority of spins cool into the same state.

Figure 27(a) shows that the rings that have a higher probability to flip tended to be grouped together in the array. The probability $\langle P_f \rangle$ that a randomly chosen ring in the array will flip after thermal cycling can be obtained from Fig. 26. It is

$$\langle P_f \rangle = \sum_{p_+} 2F(p_+)p_+(1-p_+) = 0.0744. \qquad (5.4)$$

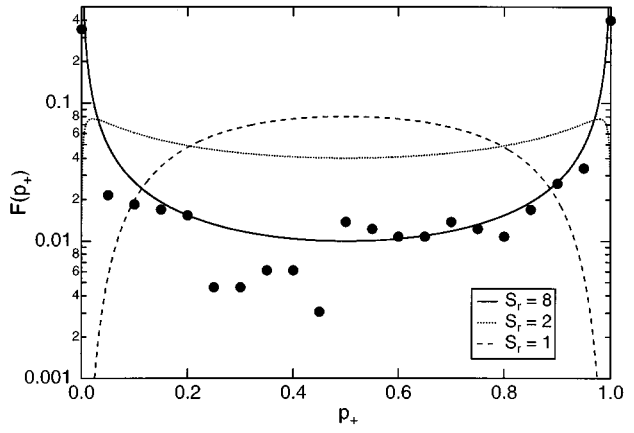

FIG. 26. Histogram of probability p_+ that a ring will cool into the spin-up state. F is fraction of a sample of 653 rings. Solid circles: data obtained from measurements of 20 cooldowns of a honeycomb lattice at $\Phi = 0.5005\Phi_0$. Curves are obtained from the model described in the text for different values of $S_r = (\mu_+ - \mu_-)\sigma_r / k_B T_f$, the ratio of the random field and thermal widths.

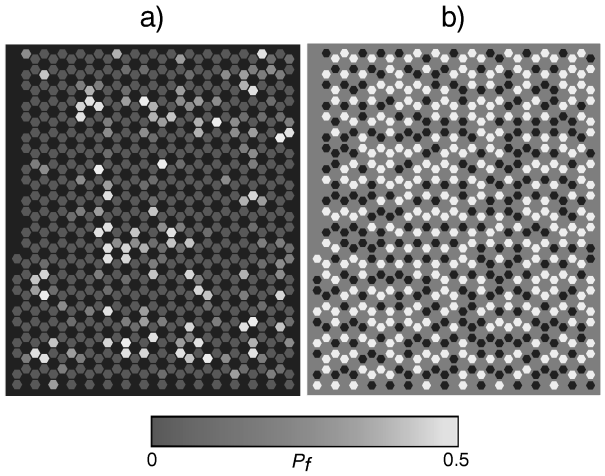

FIG. 27. (a) Grayscale map of the probability $P_f = 2p_+(1-p_+)$ that a ring changes state between two cooldowns. Data was obtained from 20 cooldowns of a region of a honeycomb lattice containing 653 rings. Black hexagons are holes in the honeycomb lattice. Scale runs from dark gray ($P_f = 0$) to white ($P_f = 0.5$). (b) Spin configuration for one of the 20 cooldowns [Fig. 25(b)]. Note the region of local Néel order that corresponds to the region of high flipping probability in (a).

From data shown in Fig. 27(a), we can calculate the correlations between flipping probabilities. For example, if a ring flips with probability $P_f \geq 0.45$, then its nearest neighbor will flip with probability 0.14, which is much larger than the average flipping probability given by Eq. (5.4). This correlation in probabilities can only come from the interaction between the rings. If a ring flips 50% of the time, then the field that it generates on its neighboring rings will fluctuate from cooldown to cooldown. This must reduce the magnitude of the random field on those rings 50% of the time, and will therefore increase their flipping probabilities.

The cluster of rings near the center Fig. 27(a) with large P_f have large local antiferromagnetic correlations. This is illustrated in Fig. 27(b), which is the spin configuration corresponding to the image in Fig. 25(b). We see that about 30 spins are in a Néel ordered state. A quantitative measure of the antiferromagnetic correlations between the rings that flip is the *weighted bond order parameter* σ', which is defined in the same manner as σ in Eq. (5.1), but with a modified measure of the antiferromagnetic bond concentration $x'_{\rm AF}$, given by

$$x'_{\rm AF} = 1/2 - \frac{1/(2N_{\rm pairs})\Sigma_{\langle i,j \rangle} s_i s_j P_f^i P_f^j}{\Sigma_{\langle i,j \rangle} P_f^i P_f^j}, \qquad (5.5)$$

where the sums run over all near-neighbor pairs. σ' thus contains no contribution from those rings which never changed their state, and weights more heavily those rings with large P_f. Averaged over the 20 cooldowns, we find that $\sigma' = -0.39 \pm 0.03$, which is much larger than the average *unweighted* bond order parameter $\sigma = -0.142 \pm 0.004$ computed for the same 20 cooldowns. This suggests that if there were no disorder, there would be long-range correlations between the spins, and that the reason for the absence of long-range order is the spread in the rings' areas, rather than freezing before the Ising ordering temperature is reached. As the

temperature is lowered, the interactions do eventually become large enough to overcome the disorder, but by then the energy barrier has grown so large that the rings cannot equilibrate into a more correlated state.

We now estimate the intrinsic thermal width relative to the disorder. This is an important question, if we want to know how much it is necessary to reduce the disorder to obtain longer range correlations. In the following analysis, we will neglect the interaction effects between the rings in Eq. (5.3), and will assume that the random field has a Gaussian distribution

$$\rho(h^r)=\frac{1}{\sigma_r\sqrt{2\pi}}\exp\left(-\frac{(h^r)^2}{2\sigma_r^2}\right), \tag{5.6}$$

where σ_r is the random field width. We can now calculate the probability *density* $G(p_+)$ that a ring will cool into the spin up state with probability p_+. Since p_+ and h_r are related by the Boltzmann distribution in Eq. (5.2), we first find h^r as a function of p_+, and then obtain $G(p_+)$ by changing variables from h^r to p_+: $G(p_+)=\rho(h^r)|dh^r/dp_+|$,

$$G(p_+)=\frac{1}{S_r\sqrt{2\pi}}\frac{1}{p_+(1-p_+)}\exp\left(-\frac{\ln^2(p_+^{-1}-1)}{2S_r^2}\right), \tag{5.7}$$

where $S_r=(\mu_+-\mu_-)\sigma_r/k_BT_f$ is the ratio of the random field and thermal widths. We also have taken $h=0$ for simplicity.

As the solid line in Fig. 26 shows, Eq. (5.7) fits our data fairly well for $S_r=8$ [after multiplying by .05 to convert $G(p_+)$ to $F(p_+)$], with most of the weight in the wings of the distribution near $p_+=0$ and $p_+=1$. Equation (5.7) is quite sensitive to S_r, however, and as the curves for $S_r=2$ and $S_r=1$ show, modest changes in S_r can radically change the probability distribution by removing the large fraction of spins that never flip and greatly increasing the fraction of rings with p_+ near 0.5. This suggests that it may be possible to achieve a significantly more correlated state through incremental improvements in the sample fabrication.

VI. SUMMARY AND CONCLUSIONS

In this work, we have opened a laboratory for low-dimensional magnetism. We have explored, using a variety of experimental probes, a two-dimensional array of electrically isolated superconducting rings. We have found that such an array is a physical realization of the 2D Ising model.

By measuring ac susceptibility, we showed that superconducting rings do behave like spins, if the applied flux is near half of a flux quantum and if the temperature is near the superconducting transition temperature. In this region of the *H-T* plane, the response of ring arrays to small field perturbations was found to be paramagnetic. The origin of the paramagnetic response is the quantization of the fluxoid, which allows a ring to have two possible orientations of its magnetic moment; the response of these moments to an external field is equivalent to the response of an Ising spin to such a field.

Susceptibility measurements showed that spins in closely spaced ring arrays interact. This interaction leads to a broadening of the susceptibility peak, as well as hysteresis in the peak position as the field is swept up and down. We have shown quantitatively how these effects are a result of the antiferromagnetic dipolar magnetic coupling between the rings.

The real-space spin configurations on four different lattices were determined by direct spatial imaging of the arrays with a scanning Hall probe microscope. The calculation of the spin-spin correlation function from the measured spin configurations showed that the correlations were antiferromagnetic and short range only. The absence of long-range order on bipartite lattices was found to be caused by quenched disorder, in the form of slight variations of the ring areas in the arrays.

Comparison of the correlation function on the square and honeycomb (bipartite) lattices, to that on the triangular and the kagomé (nonbipartite) lattices, showed that the nonbipartite lattices have weaker short-range correlations than the bipartite lattices. Thus we have a direct experimental observation of geometric frustration on Ising antiferromagnets. It is interesting that geometric frustration can be observed even in the presence of strong disorder.

There are several future projects which may warrant further development. Clearly, one would like to reduce the disorder of the ring areas. As we have seen, it appears that only a rather small reduction is likely required in order for long-range order to develop. Starting from a more ordered state at $\nu=1/2$, one could then do a detailed study of the introduction of disorder into this model system by going to higher flux fractions. It is of course also possible to explore ring arrays of lower dimensionality (i.e., 1D arrays). By fabricating parallel 1D arrays with varying interchain spacings, an entire sequence of arrays, from purely 1D, through highly anisotropic 2D arrays, to pure 2D arrays can be studied.

ACKNOWLEDGMENTS

We thank M. Höricke for technical assistance with MBE growth, and L. P. Lévy, M. Robbins, M. Tarlie, and J. Price for stimulating discussions. This work was supported by NSF Grant Nos. DMR-92-22541 and DMR-93-57518, and was performed in part at the Cornell Nanofabrication Facility which is supported by the NSF under Grant No. ECS-8619049, Cornell University and industrial affiliates. D.H.R. acknowledges the support of the David and Lucile Packard Foundation.

APPENDIX A: FLUX QUANTIZATION IN WIDE SUPERCONDUCTING RINGS

It is straightforward to show that within Ginzburg-Landau theory,[21] the free energy of an infinitesimally narrow ring of arbitrary shape is equal to

$$F_1=\epsilon_c\sigma' L\left[(2f^2-f^4)-8\pi^2f^2\frac{\xi^2}{L^2}\left(n-\frac{\Phi}{\Phi_0}\right)^2\right]+\int\frac{H^2}{8\pi}\,dV, \tag{A1}$$

where $\epsilon_c=-H_c^2/(8\pi)=\alpha\Psi_\infty^2/2$ is the condensation energy density (in terms of standard parameters in GL theory[21]), σ' is the wire cross section, L is the ring circumference, ξ is the GL coherence length, n is the fluxoid number,

$f=\Psi/\Psi_\infty$ is the normalized order parameter,[21] and Φ is the magnetic flux threading the ring. The condensation energy is the superconducting free-energy density relative to the normal state, and therefore it is negative below T_c. The rightmost term inside the square brackets represents the kinetic energy of the superconductor, and has a positive contribution to the total free energy, i.e., it reduces the magnitude of the total free energy. This term is the kinetic energy of the supercurrent. The integral on the right-hand side is the magnetic field energy of the induced currents in the ring, and it is equal to $L_s I^2/2c$, where L_s is the self-inductance and I is the current in the wire ($I=-\partial F/\partial\Phi$). Near T_c, this term is much smaller than the superconducting energy,[22] and it can be neglected. The current in the narrow ring can be obtained from the second GL equation.[21] It is

$$I_1=|\epsilon_c|\sigma' c\,\frac{(4\pi\xi)^2}{\Phi_0 L}f^2\left(n-\frac{\Phi}{\Phi_0}\right). \tag{A2}$$

To treat rings with finite wire width, we assume that f is constant, because near $T_c(\Phi)$ the coherence length ξ is larger than the wire width w and thickness d. Furthermore, we assume that the current flow lines are a scale factor times the inner ring boundary. If the ring has sharp corners, this approximation may be questioned, but comparison with our experiments showed a very good agreement between the calculations and the measurements. With these assumptions, we can calculate the free energy and current of a wide ring by integrating Eqs. (A1) and (A2) over the current flow lines. Since $\Phi(L)\sim L^2$, we see from Eq. (A2) that the current density in a wide ring is not uniform, and that the current is distributed differently in the $n=0$ and $n=1$ states. This difference in the current distribution will cause a difference in the magnetic moments of the spin up and spin down states, as we see in our magnetization measurements (Sec. IV A).

For the free energy of the wide ring, we obtain

$$F=\epsilon_c d\int_{w_1}^{w_2} dw L(w)\left[(2f^2-f^4)-8\pi^2 f^2\,\frac{\xi^2}{L^2(w)}\times\left(n-\frac{\Phi[L(w)]}{\Phi_0}\right)^2\right]. \tag{A3}$$

The integration is carried out from the inner boundary to the outer boundary. We again can neglect the self-inductive energy. The integral $\int L(w)dw=\widetilde{S}$ is just the area enclosed between the inner and outer circumferences of the wire. If we define

$$\widetilde{I}(n,H)=\int_{w_1}^{w_2} dw\,\frac{1}{L(w)}\left(n-\frac{\Phi[L(w)]}{\Phi_0}\right)^2, \tag{A4}$$

then the free energy is

$$F=\epsilon_c d[(2f^2-f^4)\widetilde{S}-8\pi^2 f^2\xi^2\widetilde{I}(n,H)]. \tag{A5}$$

The equilibrium normalized order parameter f_0 is obtained by minimizing F with respect to f. It is

$$f_0=\sqrt{1-\frac{4\pi^2\xi^2}{\widetilde{S}}\widetilde{I}(n,H)}. \tag{A6}$$

When the parameter f_0 is inserted back in to Eq. (A5), then we obtain for the free energy

$$F=\widetilde{S}\epsilon_c d f_0^4=\widetilde{S}\epsilon_c d\left(1-\frac{4\pi^2\xi^2}{\widetilde{S}}\widetilde{I}(n,H)\right)^2. \tag{A7}$$

The general expression for $T_c(H)$ is obtained by setting $f_0=0$:

$$T_c(H)=\max\{T_c(n,H)\}=\max\left\{T_c(H=0)\left(1-\frac{4\pi^2\xi^2(0)}{\widetilde{S}}\widetilde{I}(n,H)\right)\right\}. \tag{A8}$$

This formula has the Little-Parks[2] T_c oscillation in it. We can obtain the field for $\Phi_0/2$ by solving the equation

$$T_c(0,H_{1/2})=T_c(1,H_{1/2}). \tag{A9}$$

The field for a flux quantum H_1 is equal to $2H_{1/2}$. From Eq. (A8) it follows that $T_c(H_1)<T_c(0)$, because of the parabolic background superimposed on the T_c oscillations.[23]

Now we will calculate the total current and the total magnetic moment of the ring. Using the current density in Eq. (A2) $j=I_1/\sigma'$, we can calculate the total current $I=d\int j(w)dw$. The final result is

$$I=d|\epsilon_c|c\,\frac{(4\pi\xi)^2}{\Phi_0}f_0^2\widetilde{J}(n,H), \tag{A10}$$

$\widetilde{J}(n,H)$ in Eq. (A10) is a new geometric factor

$$\widetilde{J}(n,H)=\int_{w_1}^{w_2}\frac{dw}{L(w)}\left(n-\frac{\Phi[L(w)]}{\Phi_0}\right). \tag{A11}$$

The magnetic moment of the ring is given by

$$\mu=\frac{d}{c}\int_{w_1}^{w_2} j(w)S(w)dw, \tag{A12}$$

which leads to

$$\mu=d|\epsilon_c|\,\frac{(4\pi\xi)^2}{\Phi_0}f_0^2\widetilde{K}(n,H), \tag{A13}$$

with $\widetilde{K}(n,H)$ given as

$$\widetilde{K}(n,H)=\int_{w_1}^{w_2} dw\,\frac{S(w)}{L(w)}\left(n-\frac{\Phi[L(w)]}{\Phi_0}\right). \tag{A14}$$

$S(w)$ is the area enclosed by $L(w)$, so that $\widetilde{S}=S(w_2)-S(w_1)$. For a square ring with inner side a and outer side b, $w\in[a/2,b/2]$, $S=b^2-a^2$, $L(w)=8w$, $S(w)=4w^2$ and $\Phi[L(w)]=HS(w)$. For a hexagon with inner side a and outer side b, $w\in[\sqrt{3}a/2,\ \sqrt{3}b/2]$, $S=3\sqrt{3}(b^2-a^2)/2$, $L(w)=4\sqrt{3}w$, $S(w)=2\sqrt{3}w^2$, and $\Phi[L(w)]=HS(w)$. The calculation of the parameters in Eqs. (A4), (A11), and (A14), is straightforward. The results for the field $H_{1/2}$ for $\Phi_0/2$ and the other parameters are summarized in Table I.

If the applied field is $H_{1/2}$, then the total currents in the ring's two states have the same magnitude, but because the current distributions are not uniform, the magnetic moments in the two states are not the same. The magnetic moment in the $n=1$ state is smaller than the magnitude of the moment in the $n=0$ state.

*Present address: Department of Physics, Harvard University, Cambridge, MA 02138.

†Present address: Sloan Center for Theoretical Neuroscience, University of California at San Francisco, 513 Parnassus Avenue, San Francisco, CA 94143.

[1] D. Davidović, S. Kumar, D. H. Reich, J. Siegel, S. B. Field, R. C. Tiberio, R. Hey, and K. Ploog, Phys. Rev. Lett. **76**, 815 (1996).

[2] W. A. Little and R. D. Parks, Phys. Rev. Lett. **9**, 9 (1962).

[3] D. Fisher, G. Grinstein, and A. Khurana, Phys. Today **41** (12), 56 (1988).

[4] J. Z. Imbrie, Phys. Rev. Lett. **53**, 1747 (1984). J. Bricmont and A. Kupiainen, *ibid.* **59**, 1829 (1987).

[5] J. S. Langer and V. Ambegaokar, Phys. Rev. **164**, 498 (1967).

[6] D. E. McCumber and B. I. Halperin, Phys. Rev. B **1**, 1054 (1970).

[7] M. B. Tarlie, E. Shimshoni, and P. M. Goldbart, Phys. Rev. B **49**, 494 (1994).

[8] E. H. Horane, J. I. Castro, G. C. Buscaglia, and A. López, Phys. Rev. B **53**, 9296 (1996), and D. Davidović *et al.* (unpublished). Horane *et al.* do not give an explicit form for the order parameter of the intermediate state. In their notation, it is $f(s)=\tilde{f}\,\mathrm{cd}[(1-\tilde{f}^2/2)^{1/2}s|m]$, where $\mathrm{cd}(u|m)$ is a Jacobian elliptic function, and $m=\tilde{f}^2/(2-\tilde{f}^2)$.

[9] Daniel C. Mattis, *The Theory of Magnetism II* (Springer-Verlag, Berlin, 1985), p. 89, 137.

[10] R. Liebmann, *Statistical Mechanics of Periodic Frustrated Ising Systems* (Springer-Verlag, Berlin, 1986), p. 38, 77.

[11] J. Siegel, J. Witt, N. Venturi, and S. B. Field, Rev. Sci. Instrum. **66**, 2520 (1995).

[12] A. M. Chang, H. D. Hallen, L. Harriot, H. F. Hess, H. L. Kao, R. E. Miller, R. Wolfe, J. van der Ziel, and T. Y. Chang, Appl. Phys. Lett. **61**, 1974 (1992).

[13] H. D. Hallen, R. Seshadri, A. M. Chang, R. E. Miller, L. N. Pfeiffer, K. W. West, C. A. Murray, and H. F. Hess, Phys. Rev. Lett. **71**, 3007 (1993).

[14] The corresponding data for the square rings has been published previously in Ref. 1.

[15] H. B. G. Casimir and F. K. Du Pre, Physica **V**, 507 (1938).

[16] D. E. McCumber, Phys. Rev. **181**, 716 (1969).

[17] The zero-current state may also be obtained by setting $2k_s^2+m_1\Delta(k_s)/3=0$ in Eq. (5b) of Ref. 7 [M. Tarlie (private communication)].

[18] Horane *et al.* (Ref. 8) predict that this state is in fact weakly metastable. If a ring were to stay in this zero current state long enough ($\approx$ 5 min) to be scanned by the SHM, such a ring would presumably appear as a gray value intermediate between that of the standard $n=0$ and $n=1$ spins. We have observed no such states in our scans so far.

[19] J. M. Cowley, Phys. Rev. **77**, 669 (1950).

[20] J. M. Ziman, *Models of Disorder* (Cambridge University Press, Cambridge, 1979), p. 17.

[21] M. Tinkham, *Introduction to Superconductivity* (McGraw-Hill, New York, 1975), p. 111.

[22] H. J. Fink and V. Grünfeld, Phys. Rev. B **33**, 6088 (1986).

[23] R. P. Groff and R. D. Parks, Phys. Rev. **176**, 567 (1968).